Supplementary Information

Controlling electron transfer channels in a plasmonic scanning tunneling microscope junction under light excitation

Chenfang Lin,*[a] Xinyu Liu,[a] Takashi Kumagai,[c,d] Melanie Müller,[e] Martin Wolf,[e] Shuyi Liu*[b]

[a] *Key Laboratory for Micro-Nano Physics and Technology of Hunan Province, State Key Laboratory of Chemo/Biosensing and Chemometrics, Hunan Institute of Optoelectronic Integration, College of Materials Science and Engineering, Hunan University, 410082, Changsha, China.*

[b] *Wuhan National Laboratory for Optoelectronics, Huazhong University of Science and Technology, Wuhan, 430074 China*

[c] *Institute for Molecular Science, 38 NishigoNaka, Myodaiji, Okazaki 444-8585, Japan*

[d] *The Graduate University for Advanced Studies, SOKENDAI, Hayama, Kanagawa 240-0193, Japan*

[e] *Department of Physical Chemistry, Fritz-Haber Institute of the Max-Planck Society, Faradayweg 4-6, 14195 Berlin, Germany*

*Corresponding authors:
lincf@hnu.edu.cn; shuyiliu@hust.edu.cn

Content

Supplementary Information 1
1 Background theory 5
1.1 Standing-wave states in an STM junction 5
1.2 Model potential 6
1.3 Calculation of the transmission coefficient *S* 8
1.4 Determining lattice potential parameters 10
1.5 Current formula[8] 12
1.6 Determine current cross-sectional area 14
1.7 determining potential groove distance, tip protrusion radius, and tip work function 15
1.8 Contribution of backward current 16
1.9 FER-state energy shift caused by electrostatic field 18
2 Hot-electron transfer theory 19
2.1 Current formula[8] 19
2.2 Hot-electron occupation Q_n 20
2.3 comparison of the coefficient α_{abs} used in simulation and evaluated by COMSOL 21
3 Analysis of shifts between FER and plasmon-assisted FER peaks 24
4 Spectra curves in main figures 25
5 Continuous downshift of plasmon-assisted FER peaks as laser power increases or current decreases 28
6 ETC transitions from *n*=0 to *n*=1 caused by laser power or current change 29
7 Confirming the assignment of peaks labeled 1 – 4 in Fig. 4a to *n*=0 ETC 30
8 Understanding sloped background in DCS arising from *n*=2 photoemission 30
9 Comparison between experimental and simulated current – distance curves 31
10 Simulated laser-power dependence of DCS with *n*=2 ETC 33
References 34

Fig. S1 Standing-wave states in an STM junction with a bias voltage of 7.775 V and a gap distance of 2.40 nm. Simulation parameter: R_{tp}=3.2 nm. 5
Fig. S2 Image charges induced by electric potential of V applied to a sphere (a) and by an electron (labeled q_{30}) between a surface and a sphere (b). 7
Fig. S3 The effect of window functions on the transmission coefficient. 11
Fig. S4 Simulation of FER peaks with constant inner potential in Ag(111) region. (without laser excitation) 12
Fig. S5 Decomposition of electron momentum $\boldsymbol{p}$ in metal. 12
Fig. S6 STM height profiles acquired at the atomic steps at different bias voltages without laser excitation. 14
Fig. S7 Relationship between the diameter of the current cross section (D_I) and d for electron transfer channels n=0, 1 and 2. 15
Fig. S8 Effect of tip protrusion radius (R_{tp}), and tip work function (Φ_t), and potential groove distance (d_{gr}) on model potential (inserts) and the simulated differential conductance spectra. 16
Fig. S9 Simulated forward and backward current in total current and DCS 17
Fig. S10 Compare potential and FER-state energies at different tip – sample separations. 18
Fig. S11 coefficient α_{abs} as a function of d used in our simulations and predicted by COMSOL simulations. 22
Fig. S12 COMSOL model 23
Fig. S13 Spectral curves in **Fig. 3** 25
Fig. S14 Spectral curves in **Fig. 4** 26
Fig. S15 Spectral curves in **Fig. 5** 27
Fig. S16 Experimental tip displacements and simulated tip-sample separation as functions of bias voltage. 28
Fig. S17 Evolution of potential energy curves, transmission coefficients (S), tip electron distribution functions (f_t), and energy distribution of current (g) as laser power or current changes. 29
Fig. S18 Confirming the assignment of peaks labeled 1 – 4 in **Fig. 4**a to n=0 ETC. 30
Fig. S19 Current – bias voltage curves at d=1.0 nm and 1.4 nm for the simulations in Fig. 5c. 30
Fig. S20 Comparing experimental and simulated current – distance curves from **Fig. 6**

(633 nm).....31
Fig. S21 Experimental and simulated current – distance curves at an excitation wavelength of 532 nm.....32
Fig. S22 α_{abs} used in the simulations in **Fig. S21** and predicted by COMSOL with L_{tp}=1 nm, R_{tp}=2.1 nm and λ=532 nm. 33
Fig. S23 Simulated differential conductance spectra (DCS) and transition of electron transfer processes from n=0, 1, to n=2 as laser power increases corresponding to the simulations in **Fig. 5**. 33

1 Background theory

1.1 Standing-wave states in an STM junction

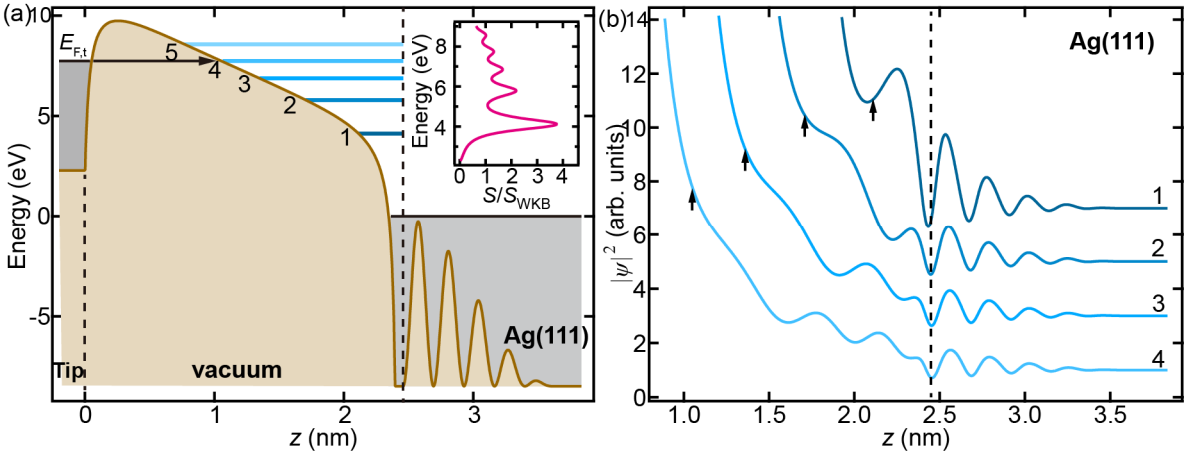

Fig. S1 Standing-wave states in an STM junction with a bias voltage of 7.775 V and a gap distance of 2.40 nm. Simulation parameter: R_{tp}=3.2 nm.

(a) potential energy (earth) across the STM junction and the corresponding standing-wave states (blue). Insert: transmission coefficient (S) relative to that in the tunneling region approximated by the Wentzel–Kramers–Brillouin (WKB) method. (b) squared magnitudes of wave functions, $|\psi|^2$, of the 1st to 4th standing-wave states. The arrows mark the boundary of the tunnel and the classically allowed regions (E_z=U), and the dashed line marks the starting point of the lattice potential at Ag(111) surface. The magnitudes of wave functions are normalized to the magnitudes at the right ends.

Fig. S1 shows the potential energy across an STM junction consisting of an Ag tip and Ag(111) sample. The slope results from the bias voltage applied to the STM junction. The five peaks in the Ag(111) part simulate the lattice potential (details in next section). Considering an electron wave function propagating from left to right, it first tunnels through the barrier. When it reaches the Ag(111) surface, a fraction is reflected due to the potential change from the vacuum to the Ag lattice. the reflected wave then interferences with the incoming wave, forming standing waves (**Fig. S1**b) and states (blue bars in **Fig. S1**a) marked by numbers 1–5. Insert of **Fig. S1**a shows total transmission coefficient divided by the transmission coefficient in the tunnel region approximated by Wentzel–Kramers–Brillouin (WKB) approximation, which roughly equals the transmission coefficient in the classically-allowed region, where the electron energy is above the potential energy. **Fig. S1**b shows that there are m maxima in squared magnitudes of wave functions for the m-th states.

1.2 Model potential

The model potential, $U(z)$, used in our simulation is:

$$U^{\mathrm{ts}}(V,d,z)=\begin{cases} U_{\mathrm{t}}, \ z\le 0 \\ E_{F,\mathrm{t}}+\Phi_{\mathrm{t}}-eV_{\mathrm{e}}(V,d,z)+U_{\mathrm{img}}(d,z), \ 0<z<d \\ U_{\mathrm{s0}}-U_{\mathrm{s1}}-eV, \ d\le z<d+d_{\mathrm{gr}} \\ \mathrm{f_{win}}\left(z-\left(d+d_{\mathrm{gr}}\right)\right)\left[U_{\mathrm{s0}}+U_{\mathrm{s1}}\sin\left(\frac{2\pi\left[z-\left(d+d_{\mathrm{gr}}\right)\right]}{d_{111}}-\frac{\pi}{2}\right)+U_{\mathrm{s1}}\right] \\ +U_{\mathrm{s0}}-U_{\mathrm{s1}}-eV, \quad d+d_{\mathrm{gr}}\le z<d+d_{\mathrm{gr}}+5d_{111} \\ U_{\mathrm{s0}}-U_{\mathrm{s1}}-eV, \ z\ge d+d_{\mathrm{gr}}+5d_{111} \end{cases}. \quad \text{(S1)}$$

It has three parts: tip, vacuum, and Ag(111). In Ag tip region (z<0), $E_{\mathrm{F,t}}$ is Fermi energy level in the tip. Φ_{s} is work function of Ag(111), which is 4.53 eV.[1] Φ_{t} is work function of tip. U_{t} is the inner potential of the tip. We apply free-electron-gas model to tip electrons, so $U_{\mathrm{t}}=E_{\mathrm{F,t}}-5.49$ eV, where 5.49 eV is Fermi energy of Ag. In vacuum gap region (0<z<d), $V_{\mathrm{e}}(V,d,z)$ is the electric potential at point z caused by the applied bias voltage, and $U_{\mathrm{img}}(d,z)$ is the image potential caused by the image charges resulting from the presence of the electron in the vacuum gap as a point charge. The potential energy in eqn (S1) is for electron transfer from the tip (z=0) to the sample (z=d), and the tip potential is fixed. For the electron transfer from the sample to the tip, we just switch the tip and the sample, and the potential becomes $U^{\mathrm{st}}(V,d,z)=U^{\mathrm{ts}}(V,d,d-z)+eV$, with sample at z=0, tip at z=d, and sample potential fixed. We acquire both V_{e} and U_{img} between a spherical protrusion on tip and Ag(111) surface using the image charge method: [2]

$$V_e(V,d,z)=V-\frac{1}{4\pi\varepsilon_0}\sum_{i=0}^{\infty}\left(\frac{q_{1i}}{\left|z'-z'_{1i}\right|}+\frac{q_{2i}}{\left|z'-z'_{2i}\right|}\right), \quad \text{(S2)}$$

where z' is transformed coordinate, z'=z_{ms}−z, with z_{ms} the position of mirror plane of the Ag(111). $z_{\mathrm{ms}}\approx d+0.35$ Å. By doing so, the Ag(111) mirror plane is at the origin of the z' coordinate system. q_{si} and z'_{si} are the charge and coordinate of the s-th series i-th image charge resulting from applying V to the tip and the sample grounded (reversed from the experimental

$$\begin{cases} z'_{10}=R+d_{\mathrm{m}} \\ q_{10}=4\pi\varepsilon_0 VR \end{cases} \qquad \begin{cases} z'_{20}=-(R+d_{\mathrm{m}}) \\ q_{20}=-4\pi\varepsilon_0 VR \end{cases} \quad \text{(S3)}$$

$$\begin{cases} z'_{1i}=R+d_m-\dfrac{R^2}{d_{2(i-1)\mathrm{C}}} \\ q_{1i}=-\dfrac{R}{d_{2(i-1)\mathrm{C}}}q_{2(i-1)} \\ d_{2(i-1)\mathrm{C}}=\left|z'_{2(i-1)}-(R+d_{\mathrm{m}})\right| \end{cases},(i\ge 1) \qquad \begin{cases} z'_{2i}=-z'_{1i} \\ q_{2i}=-q_{1i} \end{cases},(i\ge 1) \quad \text{(S4)}$$

setup, therefore causing an additional transformation by subtracting the result from V):
where R is the tip protrusion radius, ε_0 is the vacuum permittivity. d_m is the distance between the mirror surfaces of tip protrusion and Ag(111). It is slightly wider than the gap distance d, which is defined by the width at the base of the barrier. We find $d_m \approx d+0.7$ Å. $d_{2(i-1)C}$ is the distance between the image charge with subscript $2(i-1)$ and the spherical center of the tip protrusion.

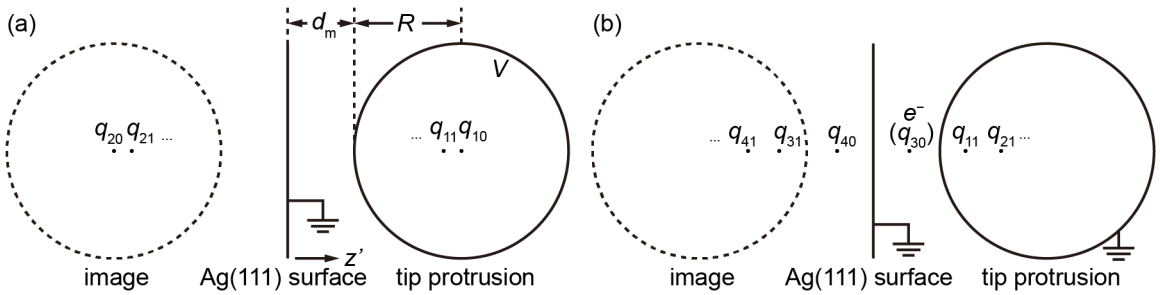

Fig. S2 Image charges induced by electric potential of V applied to a sphere (a) and by an electron (labeled q_{30}) between a surface and a sphere (b).

U_{img} is:

$$U_{\mathrm{img}}(d,z) = -\frac{e^-}{8\pi\varepsilon_0}\left\{\frac{q_{40}}{|z'-z'_{40}|} + \sum_{i=1}^{\infty}\sum_{s=1}^{4}\frac{q_{si}}{|z'-z'_{si}|}\right\}, \tag{S5}$$

where e^- is the electron charge. There is a 1/2 factor in the expression of U_{img},[3] the reason of which can be shown by the image potential on a single planar surface.[4] Imaging a planar surface at z'=0, the image force is

$$F_{\mathrm{img}} = -\frac{1}{4\pi\varepsilon_0}\frac{e^2}{(2z')^2} \tag{S6}$$

for an electron at z'. The image potential is therefore

$$U_{\mathrm{img}} = -\int_{\infty}^{z'} F_{\mathrm{img}}dz' = -\frac{1}{8\pi\varepsilon_0}\frac{e^2}{2z'}. \tag{S7}$$

Notice the 1/2 factor in the U_{img}. Since $z'-z'_{40}$ equals $2z'$, there is a 1/2 factor in the first term of expression of U_{img}. For the spherical surface, the 1/2 factor in the U_{img} is less obvious because the F_{img} becomes more complex, but we have validated the 1/2 factor through numerical integration. In all, there is 1/2 factor in all the terms of U_{img}, validating the 1/2 factor in eqn (S5). q_{si} and z'_{si} are given by

$$\begin{cases} z'_{30} = z' \\ q_{30} = e^- \end{cases} \qquad \begin{cases} z'_{40} = -z' \\ q_{40} = -e^- \end{cases} \tag{S8}$$

$$\begin{cases} z'_{1i} = (R + d_{\mathrm{m}}) - \dfrac{R^2}{d_{3(i-1)\mathrm{C}}} \\ q_{1i} = -\dfrac{R}{d_{3(i-1)\mathrm{C}}} q_{3(i-1)} \\ d_{3(i-1)\mathrm{C}} = \left| R + d_{\mathrm{m}} - z'_{3(i-1)} \right| \end{cases}, (i \geq 1) \qquad \begin{cases} z'_{2i} = (R + d_{\mathrm{m}}) - \dfrac{R^2}{d_{4(i-1)\mathrm{C}}} \\ q_{2i} = -\dfrac{R}{d_{4(i-1)\mathrm{C}}} q_{4(i-1)} \\ d_{4(i-1)\mathrm{C}} = \left| R + d_{\mathrm{m}} - z'_{4(i-1)} \right| \end{cases}, (i \geq 1) \tag{S9}$$

$$\begin{cases} z'_{3i} = -z'_{1i} \\ q_{3i} = -q_{1i} \end{cases}, (i \geq 1) \qquad \begin{cases} z'_{4i} = -z'_{2i} \\ q_{4i} = -q_{2i} \end{cases}, (i \geq 1) \tag{S10}$$

We introduce oscillating potentials according to the nearly free electron model[5] in the Ag crystal region of $U(z)$ in eqn (S1) to simulate the reflection of electron wave function at the Ag(111) surface. U_{s0} is averaged potential in Ag crystal, and U_{s1} is amplitude of oscillation before a window function $\mathrm{f_{win}}$ is applied. d_{111} is the distance between Ag(111) planes. d_{gr} is the width of the groove formed between the edges of potential barrier and lattice potential.

For the purpose of calculating transmission coefficient, we need to terminate the lattice potential and recover constant potential beyond some crystal planes in Ag crystal. For time cost considerations, we terminate the lattice potential beyond 5 Ag(111) planes. An abrupt termination results in artificial peaks in the transmission coefficient and DCS (Details in section 1.4). Therefore, $\mathrm{f_{win}}$ is applied to the lattice potential to avoid those peaks. $\mathrm{f_{win}}$ is Hann type:

$$\mathrm{f_{win}}(z) = \begin{cases} 0, & z < -\mathrm{w}/2 \text{ or } z > \mathrm{w}/2 \\ \dfrac{1}{2}\left[1 + \cos\left(\dfrac{2\pi z}{\mathrm{w}}\right)\right], & -\mathrm{w}/2 \leq z \leq \mathrm{w}/2 \end{cases}, \tag{S11}$$

where w is the base width of the window.

1.3 Calculation of the transmission coefficient *S*

To calculate the transmission coefficient S, the stationary Schrödinger equation is solved in one dimension for wave function $\psi(z)$:

$$\left[-\frac{\hbar^2}{2m}\frac{\partial^2}{\partial z^2} + U(z)\right]\psi(z) = E_z\psi(z), \tag{S12}$$

With the model potential described in section 1.2, we numerically solved the Schrödinger equation eqn (S12) using the fifth-order Runge-Kutta method provided by the IntegrateODE function in Igor Pro 9.05 to obtain the wave function $\psi(z)$. Since the potential energy is constant in both source and receiver, the wave functions are composed of plane waves. $\psi(z)$ is the superposition of an incident wave and a reflected wave in the electron source and a transmitted wave in the electron receiver. So:

$$\psi(z) = \begin{cases} A_{\mathrm{in}}e^{ik_{\mathrm{o}}z} + A_{\mathrm{R}}e^{-ik_{\mathrm{o}}z}, & z < z_1 \\ A_{\mathrm{T}}e^{ik_{\mathrm{r}}z}, & z > z_2 \end{cases} \tag{S13}$$

where A_{in}, A_R and A_T are the complex amplitude of the incident, reflected and transmitted wave, respectively. k_o and k_r are wave vectors of the electron in z direction in the source and receiver, respectively:

$$\begin{cases} k_o = \dfrac{\sqrt{2m(E_z - U_o)}}{\hbar} \\ k_r = \dfrac{\sqrt{2m(E_z - U_r)}}{\hbar} \end{cases}, \tag{S14}$$

where U_o and U_r are inner potential in the source and receiver, respectively. Since the wave function is a simple plane wave in the receiver, we start from the receiver and propagate the wave function towards the source. We set the boundaries at $z_o = -5$ Å and $z_r = d_m + 5$ Å. Therefore, the boundary condition is:

$$\begin{cases} \psi(z_r) = e^{ik_r z_r} \\ \psi'(z_r) = ik_r e^{ik_r z_r} \end{cases}, \tag{S15}$$

with A_T=1. Then, the $\psi(z)$ at $z_o \le z < z_r$ is solved numerically from z_r to z_o. Once the wave function is obtained, we acquire $\psi(z_o)$ and $\psi'(z_o)$, which are written as ψ_o and ψ'_o, respectively, for short. The transmission coefficient is calculated as following: Since $U(z)-E_z$ in eqn S12 is a negative constant in the source, both the real and imaginary part of the $\psi(z)$ can also be expressed as:

$$\psi(z) = a_1 \cos(k_o z + \varphi_1) + i a_2 \sin(k_o z + \varphi_2), (z < 0) \tag{S16}$$

so

$$\begin{cases} \psi(z_o) = a_1 \cos(k_o z_o + \varphi_1) + i a_2 \sin(k_o z_o + \varphi_2) \\ \psi'(z_o) = -a_1 k_o \sin(k_o z_o + \varphi_1) + i a_2 k_o \cos(k_o z_o + \varphi_2) \end{cases}. \tag{S17}$$

Therefore,

$$\begin{cases} \varphi_1 = \arctan\left(-\dfrac{\mathrm{Re}(\psi'_o)}{k_o \mathrm{Re}(\psi_o)}\right) - k_o z_o \\ a_1 = \dfrac{\mathrm{Re}(\psi_o)}{\cos(k_o z_o + \varphi_1)} \end{cases} \qquad \begin{cases} \varphi_2 = \arctan\left(\dfrac{k_o \mathrm{Im}(\psi_o)}{\mathrm{Im}(\psi'_o)}\right) - k_o z_o \\ a_2 = \dfrac{\mathrm{Im}(\psi_o)}{\sin(k_o z_o + \varphi_2)} \end{cases} \tag{S18}$$

Connecting eqn S13 and eqn S16, we obtain A_{in} and A_R:

$$\begin{cases} A_{in} = \dfrac{1}{2}\left(a_1 e^{i\varphi_1} + a_2 e^{i\varphi_2}\right) \\ A_R = \dfrac{1}{2}\left(a_1 e^{-i\varphi_1} - a_2 e^{-i\varphi_2}\right) \end{cases} \tag{S19}$$

The transmission coefficient is the ratio between the probability fluxes of the transmitted and the incident waves:

$$S = \frac{v_r}{v_o}\frac{|A_T|^2}{|A_{in}|^2} = \frac{k_r}{k_o}\frac{|A_T|^2}{|A_{in}|^2} = \frac{k_r}{k_o}\frac{1}{|A_{in}|^2}, \tag{S20}$$

where $v_{o(r)}$ is the velocity of the wave in the electron source (receiver). $v_{o(r)} = \hbar k_{o(r)}/m$.

To visualize the enhanced transmission coefficient through the FER states, the transmission coefficient is viewed as

$$S = S_{CFR} S_{CAR}, \tag{S21}$$

where S_{CFR} and S_{CAR} stand for the transmission coefficient of the classically forbidden ($U(z)<E_z$, shaded region below the potential energy curve in **Fig. S1**a and Fig. 2d) and allowed ($U(z)\geq E_z$, the region above the potential energy curve) region, respectively. Therefore, $S_{CAR} = S/S_{CFR} \approx S/S_{WKB}$, where S_{WKB} is the transmission coefficient of the classically forbidden region approximated by the Wentzel–Kramers–Brillouin (WKB) method:

$$S_{WKB} = \exp\left(-\frac{2\sqrt{2m}}{\hbar}\int_{z_1}^{z_2}\sqrt{U(z)-E_z}dz\right), \tag{S22}$$

where z_1 and z_2 are the positions where E_z and $U(z)$ intersect. The inset of **Fig. S1**a and Fig. 2d plots S/S_{WKB}. Peaks appear in S/S_{WKB} when E_z matches the energy of FER states. Therefore, when bias voltage matches the energy of FER states, peaks appear in DCS, forming the FER peaks.

1.4 Determining lattice potential parameters

In nearly free electron mode, lattice potential is approximated by a sin wave. **Fig. S3**a shows a sin wave with 10 periods. There is abrupt cutoff at both ends. Since we are only interested in the transmission coefficient through the potential at $z>0$, **Fig. S3**b shows that by taking the square root of the transmission coefficient through the full space. A band gap opens up at −0.5 to 3.9 eV, resembling the bulk *L*-gap for Ag(111) faces.[6] However, there are undesired peaks in the transmission coefficient at $E>4$ eV due to the interference between the incoming electron wave and the reflected electron wave at the boundary where the lattice potential is cut off. If we apply such lattice potentials, FER peaks at $V<6$ V are overwhelmed by those artifact peaks (red arrows) in the simulated DCS (**Fig. S3**c). Therefore, a smooth window function is applied to the lattice potential, leading to the potential in **Fig. S3**d. Notice that the part at z>0 is used in the model potential. **Fig. S3**e plots the transmission coefficient for the z>0 part, showing no undesired peaks at $E>4$ eV. **Fig. S3**f shows the simulated DCS with all FER peaks visible.

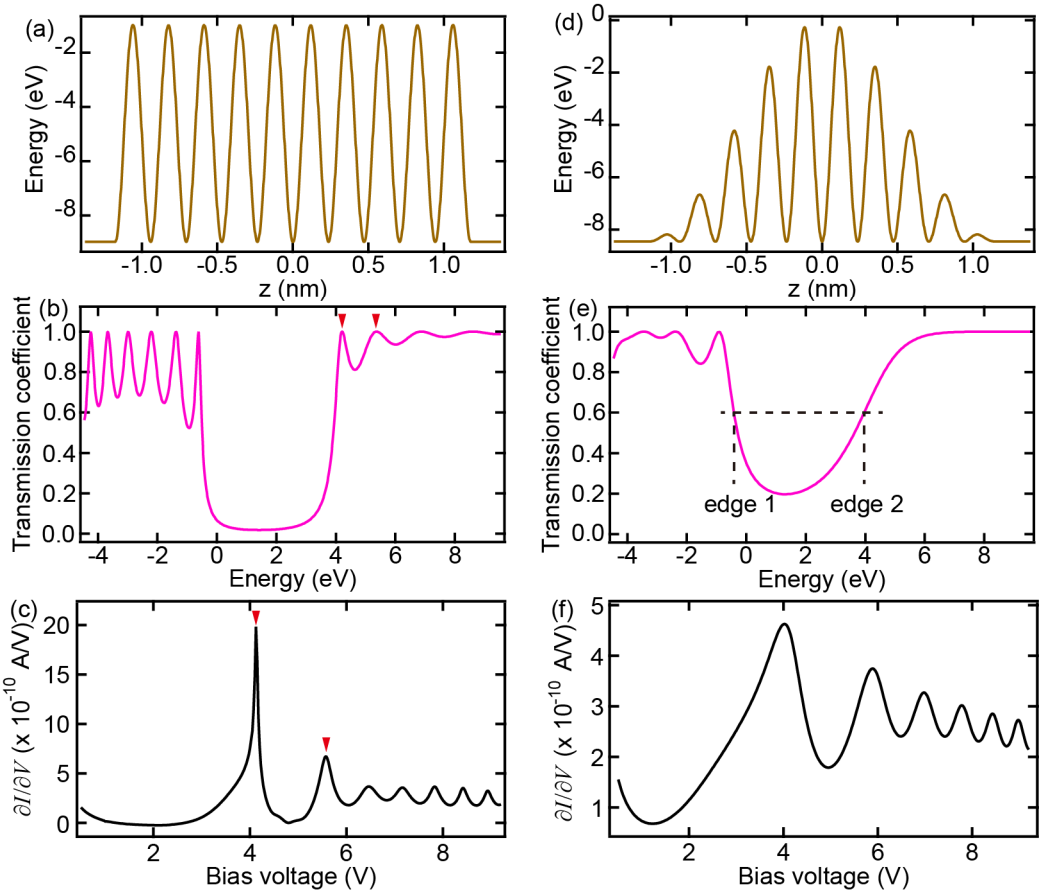

Fig. S3 The effect of window functions on the transmission coefficient.

(a, d) The lattice potential multiplying a rectangular (a) and a Hann window (d). (b, e) Transmission coefficients for half space (z>0) in (a, c), respectively. All energies are relative to the Fermi level. (c, f) Simulated DCS of the STM junction without laser excitation for the experimental data Fig. 2a using lattice potential at z>0 shown in (a) and (d), respectively.

The parameters of the potential, U_{s0} and U_{s1}, are determined to be −4.26 eV relative to the Fermi level and 4.2 eV so that the bulk L gap for Ag(111) faces is reproduced at the right position from −0.4 to 3.9 eV (**Fig. S3**e, edge 1 and 2).[7]

We add here that the successful fit to the FER peaks without laser excitation in Fig. 2a cannot be achieved without the application of oscillating potentials in Ag(111) region. **Fig. S4** shows simulated DCS applying constant inner potential, $U_s = E_{F,s} - 5.49$ eV, where 5.49 eV is Fermi energy of Ag, in Ag(111) region (free electron gas model). The match between simulated and experimental FER peaks cannot be achieved whatever R_{tp} is.

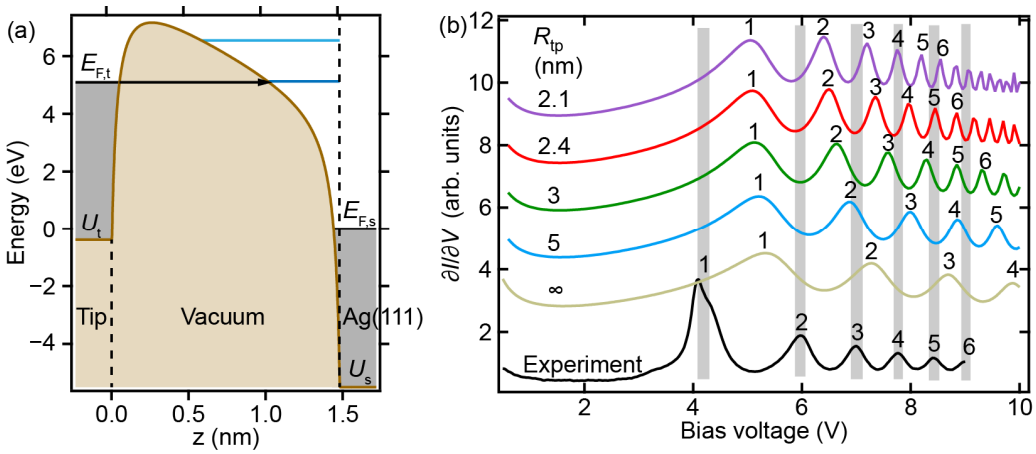

Fig. S4 Simulation of FER peaks with constant inner potential in Ag(111) region. (without laser excitation)

(a) Potential energy (earth) across the STM junction and the corresponding standing-wave states (blue) at V=5.1 V, d=1.48 nm, and R_{tp}=2.4 nm. (b) Simulated FER peaks with different R_{tp} compared with experimental ones.

1.5 Current formula[8]

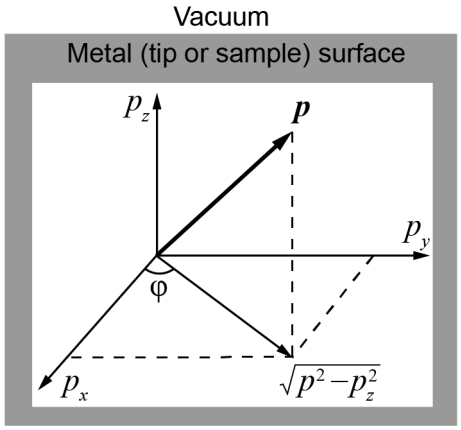

Fig. S5 Decomposition of electron momentum $\boldsymbol{p}$ in metal.

Without laser illumination, the current is

$$I(V,d) = I^{+}(V,d) - I^{-}(V,d), \tag{S23}$$

where $^+$ and $^-$ denote electron transfer from the tip to the Ag(111) sample and vice versa. "t" and "s" denote the tip and the sample, respectively. Both I^+ and I^- are calculated in momentum space from a free electron gas:[9]

$$I^{+(-)}(V,d) = \frac{2eA_I(d)}{h^3}\int_0^{+\infty}\int_{-\infty}^{+\infty}\int_{-\infty}^{+\infty}\frac{p_{z,o}}{m}f_o(E)S(V,d,E_z)dp_x\,dp_y\,dp_{z,o}\,, \tag{S24}$$

where e is the elementary charge, A_I is the lateral area of the current and is a function of d, h is the Planck constant, and m is the electron mass. p_x and p_y are the electron momentum in the x

and y direction. Because we use a 1D potential that only varies in the z-direction, p_x and p_y are invariant across the junction. $p_{z,o}$ is the z-direction momentum in the electron source, which refers to the tip for I^+ and the sample for I^-. E and E_z are the total energy eigenvalue and the energy eigenvalue in z-direction, respectively. $f_o(E)$ is the electron energy distribution functions in the source. S is the energy-dependent transmission coefficient.

Then we show step by step how to transform eqn S24 to the energy space by substituting p_x, p_y, and p_z with E, φ, and E_z. We first decompose electron momentum in the source (p_o) in Cartesian coordinate system (**Fig. S5**):

$$\begin{cases} p_x = \sqrt{p_o^2 - p_{z,o}^2}\cos\varphi \\ p_y = \sqrt{p_o^2 - p_{z,o}^2}\sin\varphi \end{cases}, \tag{S25}$$

where "o" denotes the electron source. Inside the source electrode, there is:

$$\begin{cases} E = \dfrac{p_o^2}{2m} + U_o \\ E_z = \dfrac{p_{z,o}^2}{2m} + U_o \end{cases}, \tag{S26}$$

so

$$\begin{cases} p_x = \sqrt{2m(E - E_z)}\cos\varphi \\ p_y = \sqrt{2m(E - E_z)}\sin\varphi \\ p_{z,o} = \sqrt{2m(E_z - U_o)} \end{cases}, \tag{S27}$$

where U_o is the potential energy in the electron source. The relationship between the volume element in the momentum space and that in the energy space is, therefore:

$$dp_x dp_y dp_{z,o} = \left|\frac{\partial(p_x, p_y, p_{z,o})}{\partial(E, \varphi, E_z)}\right| = m\sqrt{\frac{m}{2(E_z - U_o)}}\, dE d\varphi dE_z, \tag{S28}$$

where $\left|\frac{\partial(p_x,p_y,p_{z,o})}{\partial(E,\varphi,E_z)}\right|$ is the Jacobian determinant. So, eqn S24 becomes

$$I^{+(-)}(V,d) = \frac{2meA_I}{h^3}\int_{U_o}^{+\infty}\int_0^{2\pi}\int_{E_z}^{+\infty} f_o(E)S(V,d,E_z)dE\, d\varphi\, dE_z \tag{S29}$$

Integrating for φ:

$$I^{+(-)}(V,d) = \frac{4\pi meA_I}{h^3}\int_{U_o}^{+\infty}\int_{E_z}^{+\infty} f_o(E)S(V,d,E_z)dE\, dE_z \tag{S30}$$

This result is essentially the same as the STM current formula deduced by Simmons.[10]

Changing the order of integration:

$$I^{+(-)}(V,d) = \frac{4\pi meA_I}{h^3}\int_{U_o}^{+\infty}\int_{U_o}^{E} f_o(E)S(V,d,E_z)\,dE_z dE \tag{S31}$$

This equals to:

$$I^{+(-)}(V,d) = \frac{4\pi meA_I}{h^3}\int_{U_o}^{+\infty} f_o(E)\int_{U_o}^{E} S(V,d,E_z)\,dE_z dE \tag{S32}$$

The above integrals are calculated numerically.

1.6 Determine current cross-sectional area

The current cross-sectional area (A_I) is

$$A_I = \pi\left(\frac{D_I}{2}\right)^2, \tag{S33}$$

where D_I is the diameter of the current cross section, which is determined roughly by the 10%–90% rise width in height profiles acquired on atomic steps **Fig. S6**. The dependency between D_I and d can be acquired through STM images at different V. The d value corresponding to each voltage can be acquired from the tip-displacement–V curve using a starting d value of ~0.7 nm.

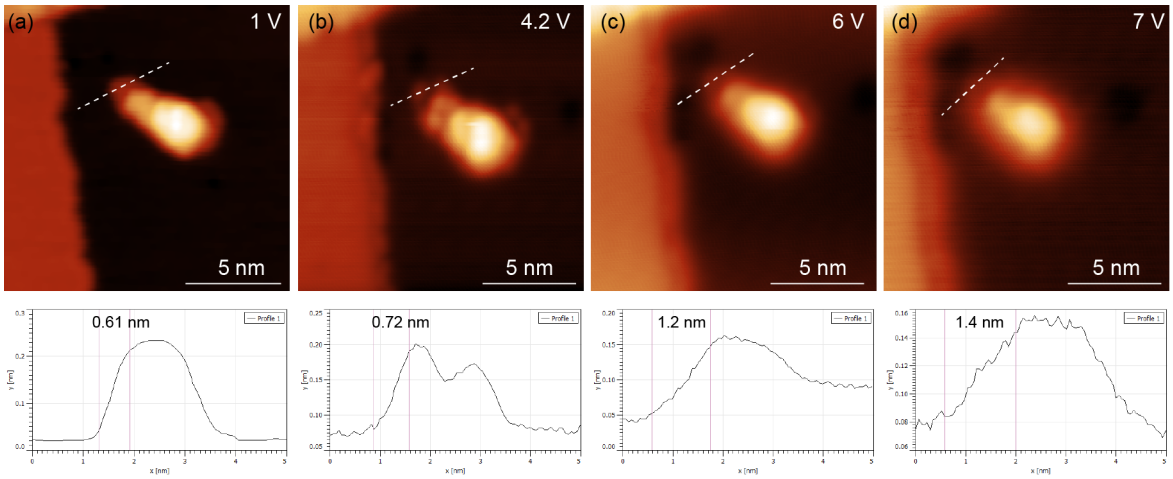

Fig. S6 STM height profiles acquired at the atomic steps at different bias voltages without laser excitation.

Fig. S7 shows the diameter of the current cross section (D_I) for dark, n=1, and n=2 ETC current measured in experiments. D_I increase with d and also n. In **Fig. S7**b, the measured D_I for n=2 ETC current (dashed) exceeds the diameter of the tip protrusion (D_{tp}) and should be interpreted as the diameter on the sample side. On the tip side, the D_I should rise towards its upper limit, that is D_{tp}. D_{tp} =5.2 nm in the case of the simulations in Figs. 5–7. We assume that D_I for n=1 ETC current also saturates at d≈2.2 nm in **Fig. S7**a because the D_I for n=1 and n=2

ETC are corelated in order to fit the outcome to the experiments in Fig. 5 and 6, which contains both n=1 and n=2 ETC current.

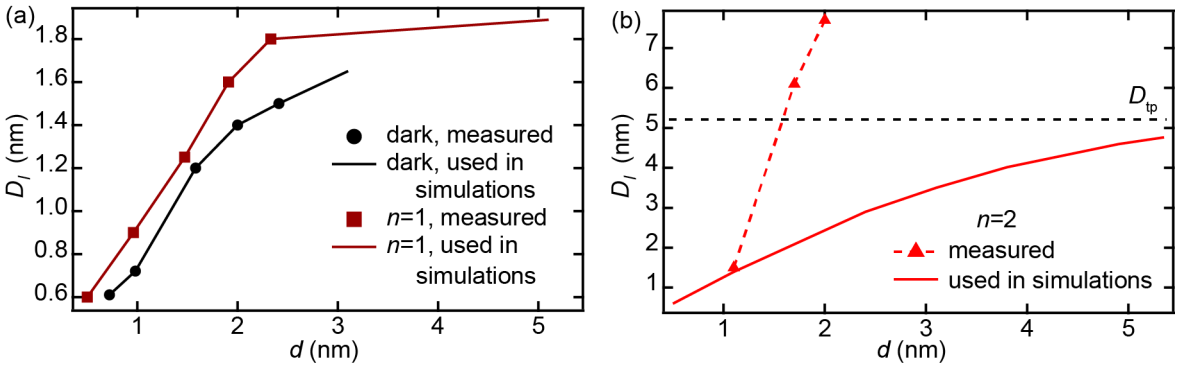

Fig. S7 Relationship between the diameter of the current cross section (D_I) and d for electron transfer channels n=0, 1 and 2.

1.7 determining potential groove distance, tip protrusion radius, and tip work function

Potential groove distance (d_{gr}) and tip protrusion radius (R_{tp}) are determined by fitting simulated DCS to the experimental DCS without laser excitation. The DCS are simulated using the Fermi–Dirac distribution:

$$f_{t(s)}(E) = \left[\exp\left(\frac{E - E_{F,t(s)}}{k_B T}\right) + 1\right]^{-1}, \tag{S34}$$

where "t" and "s" stand for the tip and the Ag(111) sample, respectively, and $E_{F,t(s)}$ stands for Fermi energy level in the tip (sample). $E_{F,t} = E_{F,s} + eV$.

Fig. S8 shows effect of R_{tp}, Φ_t, and d_{gr} on model potential and the simulated differential conductance spectra. In the following comparisons, we fix sample Fermi level. Increasing R_{tp} or Φ_t rise the slope in the middle part of potential energy [see inserts in **Fig. S8**(a, b)]. As a result, the distances between adjacent FER peaks increase according to Stark effect while the position of first FER peak barely changes. Since R_{tp} or Φ_t have similar effects on FER peak positions, we fix Φ_t and tune R_{tp}. We fix Φ_t at 4.48 eV in all simulations. This value is arbitrary as long as it is slightly smaller than Φ_s=4.53 eV, because work function of Ag(111) is the highest among all surface orientations.[1] Increasing d_{gr} causes a different effect on FER peaks: that is downshift of all FER peaks—a behavior like the energy levels in a potential well—while the distances between adjacent FER peaks barely change. Therefore, by tuning R_{tp} and d_{gr}, the positions of third to fifth peaks can be fitted to the experiments in Fig. 2a with R_{tp}=3.7 nm and d_{gr}=60 pm. Since d_{gr} value belongs to a property of Ag(111) surface, it is kept 60 pm in all simulations.

In literature, distance between a crystal surface, defined as the edge of the oscillating potential, and the image plane, d_m, and distance between the image plane to the corner of the barrier, d_c, are often talked about. $d_{gr} = d_m + d_c$. In our model, there is d_c=25 pm and d_m=35 pm. The d_m value is larger than that (=15 pm) found for Ag(001) surface,[5] possibly explained by the finding that d_m for Ag(111) is 17 pm larger than that for Ag(001).[11]

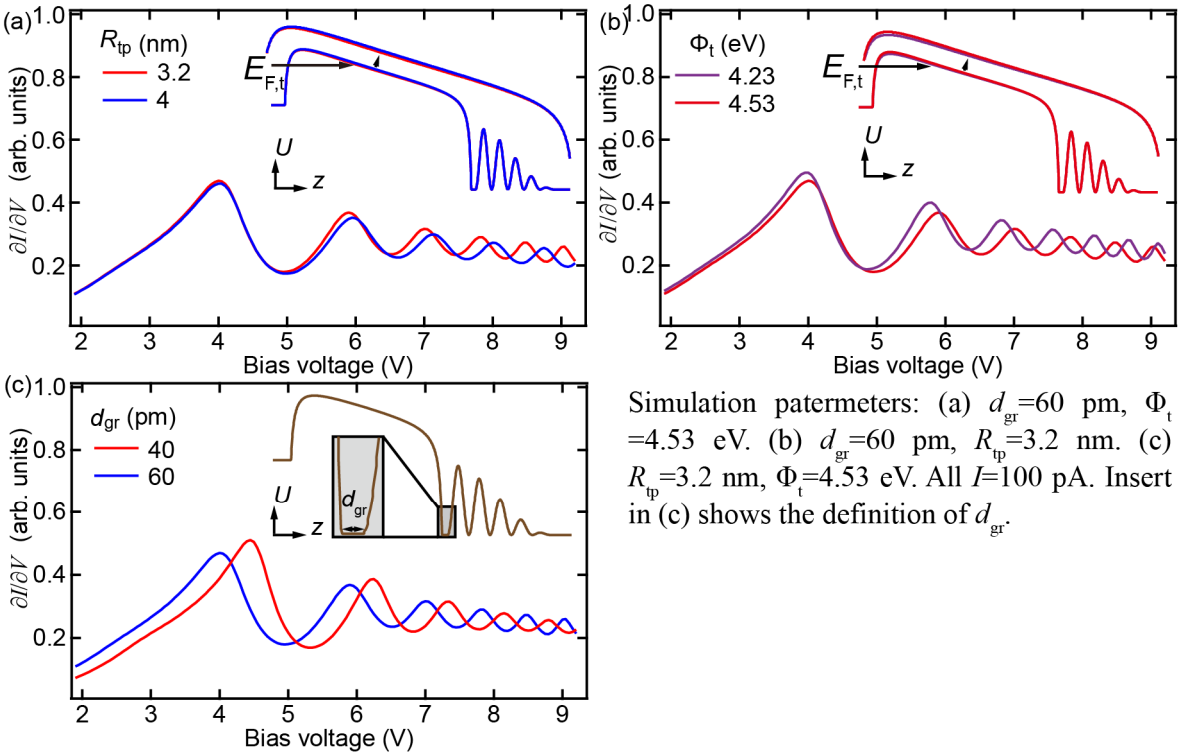

Simulation patermeters: (a) d_{gr}=60 pm, Φ_t =4.53 eV. (b) d_{gr}=60 pm, R_{tp}=3.2 nm. (c) R_{tp}=3.2 nm, Φ_t=4.53 eV. All I=100 pA. Insert in (c) shows the definition of d_{gr}.

Fig. S8 Effect of tip protrusion radius (R_{tp}), and tip work function (Φ_t), and potential groove distance (d_{gr}) on model potential (inserts) and the simulated differential conductance spectra.

1.8 Contribution of backward current

In eqn (1), current is forward current I^+ minus backward current I^-. The contribution of I^- is examined here. **Fig. S9**(a and b) show that the contribution of I^- is negligible at V>2.5 V without laser excitation. **Fig. S9**(c and d) show that the contribution of I^- is negligible at V>1.9 V with laser excitation. At V<2.5 V or 1.9 V, both I^+ and I^- increase rapidly as bias voltage approaches zero, because d continues to decrease in constant current mode.

From eqn (1), we know

$$\frac{\partial I}{\partial V} = \frac{\partial I^+}{\partial V} - \frac{\partial I^-}{\partial V}. \qquad \text{(S35)}$$

Since the partial derivations are evaluated under fixed d, in the free electron model, $\partial I^+/\partial V$ is always positive and $\partial I^-/\partial V$ negative, because I^+ always increases and I^- decreases as bias voltage increases. In **Fig. S9**(b and d), as bias voltage approaches zero, $\partial I^+/\partial V$ approaches zero while $\partial I^-/\partial V$ becomes negative and diverges. As a result, $\partial I/\partial V$ bends upwards as bias voltage approaches zero. In **Fig. S9**b, negative $\partial I^+/\partial V$ at V=0.5 V is due to the bulk L-gap of Ag. We find that in constant-d mode, I^+ decreases as bias voltage increases near V=0 because the transmission coefficient in Ag crystal decreases as energy increases near the Fermi level of Ag crystal (**Fig. S3**e).

Under laser excitation, we find in **Fig. S9**c that the backward current from excited electrons in sample, I_1^-, is negligible in our measurement range, and I^- is dominated by I_0^-. This is consistent with the reasoning in **Fig. S17**, i.e., at small d, tunneling of unexcited electrons tends to dominate over tunneling of photoexcited electrons. At V<2 V, d<1 nm. At such small d, a hot electron occupation of ~ 3×10^{-4} (**Fig. S11**a) is just not enough to compete with unexcited electrons in the sample.

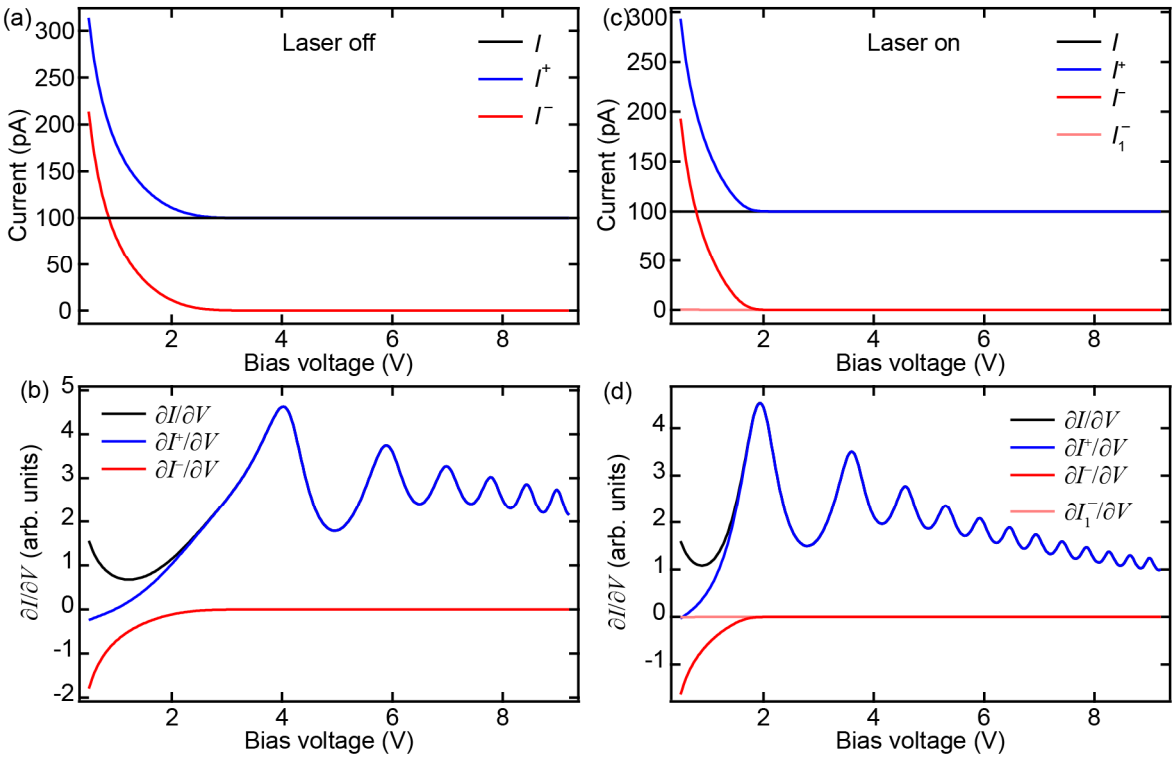

Fig. S9 Simulated forward and backward current in total current and DCS (a, b) for the case in Fig. 2a. (c, d) for the case in Fig. 2b.

1.9 FER-state energy shift caused by electrostatic field

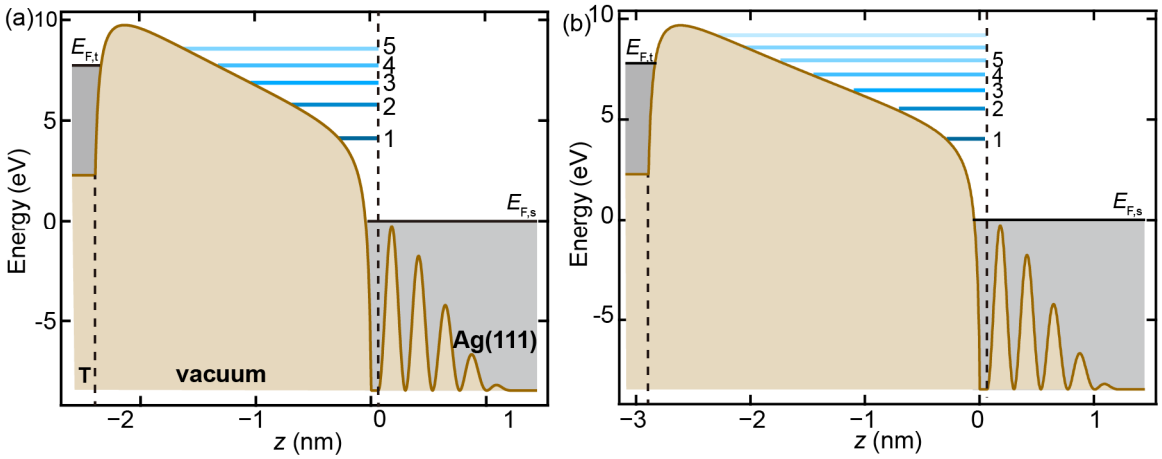

Fig. S10 Compare potential and FER-state energies at different tip–sample separations. (a) d=2.40 nm (b) d=2.90 nm. Both: V=7.775 V. R_{tp}=3.2 nm.

Electrostatic field in STM junction has pronounced effect on energies of the second to higher-number FER states. **Fig. S10** compares potential energy and FER states at two electrostatic-field strength caused by varying gap distance. Increasing gap distance leads to decrease of electrostatic-field strength, resulting in decrease of energy of FER states. **Table S1** lists the energy downshifts of first to fifth states. The higher the number, the larger the shift. This phenomenon is the same as that in a triangular potential well.[12]

Table S1. energy shift of the m-th state between d=2.40 nm and 2.90 nm.

m	**1**	**2**	**3**	**4**	**5**
Shift (eV)	0.1	0.28	0.38	0.53	0.65

2 Hot-electron transfer theory

2.1 Current formula[8]

Under illumination with optical power P, the current can be expressed in three ETCs of n=0,1, and 2[8]

$$I(V,d,P) = I_0(V,d) + I_1(V,d,P) + I_2(V,d,P) \tag{S36}$$

where

$$I_0(V,d) = I_0^+(V,d) - I_0^-(V,d) \tag{S37}$$

$$I_n(V,d,P) = I_n^+(V,d,P) - I_n^-(V,d,P), \qquad (n = 1,2) \tag{S38}$$

$$I_0^{+(-)}(V,d) = \frac{4\pi meA_{I0}(d)}{h^3}\int_{U_{\mathrm{t(s)}}}^{+\infty} f_{\mathrm{t(s)}0}(E)\int_{U_{\mathrm{t(s)}}}^{E} S(V,d,E_z)\,dE_z dE \tag{S39}$$

$$I_n^{+(-)}(V,d,P) = \frac{4\pi meA_{In}(d)}{h^3}\int_{U_{\mathrm{t(s)}}}^{+\infty} f_{\mathrm{t(s)}n}(d,E,\mathrm{P})\int_{U_{\mathrm{t(s)}}}^{E} S(V,d,E_z)\,dE_z dE\,, (n = 1,2), \tag{S40}$$

where I^+ and I^- consider the transfer of tip electron to sample and vice versa, respectively. d is the tip–sample separation, A_{In} is cross-sectional area of the current in n-th ETC, $U_{\mathrm{t(s)}}$ is the inner potential of the tip (sample), S is the transmission coefficient, E is the total energy, E_z is kinetic energy in the z-direction added to the potential energy. $f_{\mathrm{t(s)}n}$ is the distribution function of the Ag tip (Ag(111) sample) resulting from n-photon absorption:[13]

$$f_{\mathrm{t(s)}0}(E) = \left[\exp\left(\frac{E - E_{\mathrm{F,t(s)}}}{k_{\mathrm{B}}T_0}\right) + 1\right]^{-1}, \tag{S41}$$

$$f_{\mathrm{t(s)}1}(d,E,P) = Q_{\mathrm{t(s)}1}(d,P)\big[\big(1 - f_0(E)\big)f_0(E - \hbar\omega) - \big(1 - f_0(E + \hbar\omega)\big)f_0(E)\big], \tag{S42}$$

$$f_{\mathrm{t(s)}2}(d,E,P) = Q_{\mathrm{t(s)}2}(d,P)\big[\big(1 - f_0(E - \hbar\omega)\big)f_0(E - 2\hbar\omega) - \big(1 - f_0(E)\big)f_0(E - \hbar\omega)\big]. \tag{S43}$$

In eqn (S42) and (S43), "t(s)" in f_0 is omitted for simplicity. f_0 is the Fermi–Dirac distribution with T_0 an effective temperature representing the low-energy Drude response through Joule heating. T_0 is set to 78 K and we have confirmed that choice of T_0 value between 8 K and 150 K has negligible effect on simulated current and DCS. k_{B} is Boltzmann constant. $E_{\mathrm{F,t(s)}}$ is the Fermi energy level in the tip (sample). $f_{\mathrm{t(s)}1}(E)$ simply forms a positive plateau at $E_{\mathrm{F,t(s)}} \le E \le E_{\mathrm{F,t(s)}} + \hbar\omega$ with occupation $Q_{\mathrm{t(s)}1}$ resulting from one-photon absorption and a negative plateau at $0 \le E \le E_{\mathrm{F,t(s)}}$ with value $-Q_{1,\mathrm{t(s)}}$ representing the holes left after the electron is excited. $Q_{\mathrm{t(s)}1}$ is:

$$Q_{\mathrm{t(s)}1}(d,P) = \frac{4E_{\mathrm{F}}\tau_{ee}\alpha_{\mathrm{abs,t(s)}}(d)}{3\pi r_{\mathrm{f}}^2 n_e \hbar^2\omega^2}P, \tag{S44}$$

where E_{F} is the Fermi energy of Ag, E_{F}=5.49 eV, τ_{ee} is the electron–electron relaxation time,

τ_{ee}≈350 fs,[14] $\alpha_{abs,t}$ and $\alpha_{abs,s}$ are coefficients measuring light absorption in the tip protrusion and the local sample region relevant to STM junction, respectively. $\alpha_{abs,t(s)}$ is a function of d. $\alpha_{abs,t}(d)$ affects the positions of the plasmon assisted FER peaks by affecting d under given I, V and P. Therefore, $\alpha_{abs,t}(d)$ is tuned to match the simulated positions of the plasmon assisted FER peaks with the experimental ones. $\alpha_{abs,t}(d)$ for each simulation is provided in **Fig. S11**. The r_f is the radius of the focal spot, n_e is the electron density of Ag, $\hbar$ is the reduced Planck constant, ω is the angular frequency of laser. Details about derivation of eqn S44 are in next section.

Similarly, $f_2(E)$ forms a positive plateau at $E_F + \hbar\omega \leq E \leq E_F + 2\hbar\omega$ with occupation Q_2 resulting from electron absorbing two photons and a negative plateau at $E_F \leq E \leq E_F + \hbar\omega$ representing the holes left after the electron was excited by the second photon. We assume $Q_2 = Q_1^2$.[15] I_2 is included only in simulations for experiments where n=2 ETC occurs.

2.2 Hot-electron occupation Q_n

The hot-electron occupation Q_1 is estimated from the number of photons absorbed:[16]

$$Q_1 = \frac{n_{ph}}{n_{sta}}, \tag{S45}$$

where "t" and "s" denote the Ag tip and the Ag(111) sample, respectively (the same as below), n_{ph} is the number of photons absorbed per unit volume and n_{sta} is the number of states per unit volume,

$$n_{sta} = \rho\hbar\omega, \tag{S46}$$

where ρ is density of states (DOS), and $\hbar\omega$ is the energy of a photon. For Ag excited by 532- or 633-nm laser, the transition is intra *sp* band. As ρ is relatively flat within the *sp* band, it is approximated by the DOS at the Fermi energy:

$$\rho \approx \frac{3}{2}\frac{n_e}{E_F}, \tag{S47}$$

where n_e is the electron density of Ag, n_e≈5.86×10^{28} m^{-3}, and E_F is the Fermi energy of Ag, E_F=5.49 eV.

$$n_{ph} = \frac{\overline{D}_{abs}\tau_{ee}}{\hbar\omega} \tag{S48}$$

where τ_{ee} is the electron–electron relaxation time, τ_{ee}≈350 fs,[14] and $\overline{D}_{abs}$ is the power absorbed per unit volume averaged in region of interest,

$$\begin{cases} \overline{D}_{abs,t} = \dfrac{1}{V_{tp}} \iiint_{V_{tp}} D_{abs}(\boldsymbol{r}) dr^3 \\ \overline{D}_{abs,s} = \dfrac{1}{V_s} \iiint_{V_s} D_{abs}(\boldsymbol{r}) dr^3 \end{cases}, \tag{S49}$$

where $D_{abs}(\boldsymbol{r})$ is the power absorbed per unit volume at point $\boldsymbol{r}$, V_s and V_{tp} is the volume of the region relevant to the hot electron transfer in the sample and the tip protrusion, respectively (see next section). In linear absorption, $\overline{D}_{\mathrm{abs}} \propto I_{\mathrm{laser}}$, where I_{in} is the incident light intensity, laser intensity at the focus, so we define

$$\alpha_{\mathrm{abs}} \equiv \frac{\overline{D}_{\mathrm{abs}}}{I_{\mathrm{in}}}, \tag{S50}$$

which is independent of the laser intensity. To help understand the α_{abs} we defined, imaging a special case where one-dimensional light propagates through a material, one can prove

$$\frac{\overline{D}_{\mathrm{abs}}}{I_{\mathrm{in}}} = \frac{1 - e^{-\alpha L}}{L}, \tag{S51}$$

where L is the length light travels, and α is absorption coefficient. When $\alpha L \ll 1$, $\alpha_{abs} \approx \alpha$. Since the $D_{abs}(\boldsymbol{r})$ is not uniform in our case, and $\overline{D}_{\mathrm{abs}}$ is defined in a small region of interest, α_{abs} measures local absorption and should not be regarded as absorption coefficient, which is a measure of material property.

Up to now, we have

$$Q_1 = \frac{2E_{\mathrm{F}}\tau_{ee}\alpha_{\mathrm{abs}}}{3n_e\hbar^2\omega^2} I_{\mathrm{in}}. \tag{S52}$$

In our experiment, I_{in} equals laser intensity at the focus, so

$$I_{\mathrm{in}} = \frac{2P}{\pi r_{\mathrm{f}}^2}, \tag{S53}$$

where P is laser power, and r_f is the radius of the focal spot (waist of a Gaussian beam). r_f roughly equals to 3λ, where λ is laser wavelength, in our setup. α_{abs} is the absorption cross section per unit volume. In all, the Q_1 is

$$Q_1 = \frac{4E_{\mathrm{F}}\tau_{ee}\alpha_{\mathrm{abs}}}{3\pi r_{\mathrm{f}}^2 n_e\hbar^2\omega^2} P. \tag{S54}$$

Specifically,

$$Q_{1,\mathrm{t(s)}}(d,P) = \frac{4E_{\mathrm{F}}\tau_{ee}\alpha_{\mathrm{abs,t(s)}}(d)}{3\pi r_{\mathrm{f}}^2 n_e\hbar^2\omega^2} P, \tag{S55}$$

where "t" and "s" denote the Ag tip and the Ag(111) sample, respectively. Both $Q_{1,t(s)}$ and $\alpha_{abs,t(s)}$ are functions of d.

2.3 comparison of the coefficient α_{abs} used in simulation and evaluated by COMSOL

In our simulations, $\alpha_{t,abs}(d)$ is a free parameter and is tuned to match the simulated positions of the plasmon assisted FER peaks to the experimental ones, because $\alpha_{t,abs}$ affects Q_{t1}, Q_{t1} affects d under constant current (equivalent to Q_{t1} affecting current under constant d), and

d affects positions of standing-wave states, so are the FER peak positions. $\alpha_{s,abs}(d)$ has negligible effect on DCS because the current is dominated by I^+. Therefore, $\alpha_{s,abs}(d)$ is determined by $\frac{\alpha_{t,abs}}{\alpha_{s,abs}} = \frac{\alpha_{t,abs}^{COMSOL}}{\alpha_{s,abs}^{COMSOL}}$, where $\alpha_{t(s),abs}^{COMSOL}$ is α acquired by COMSOL (see below). **Fig. S11** show the $\alpha_{abs}(d)$ used by the main figures.

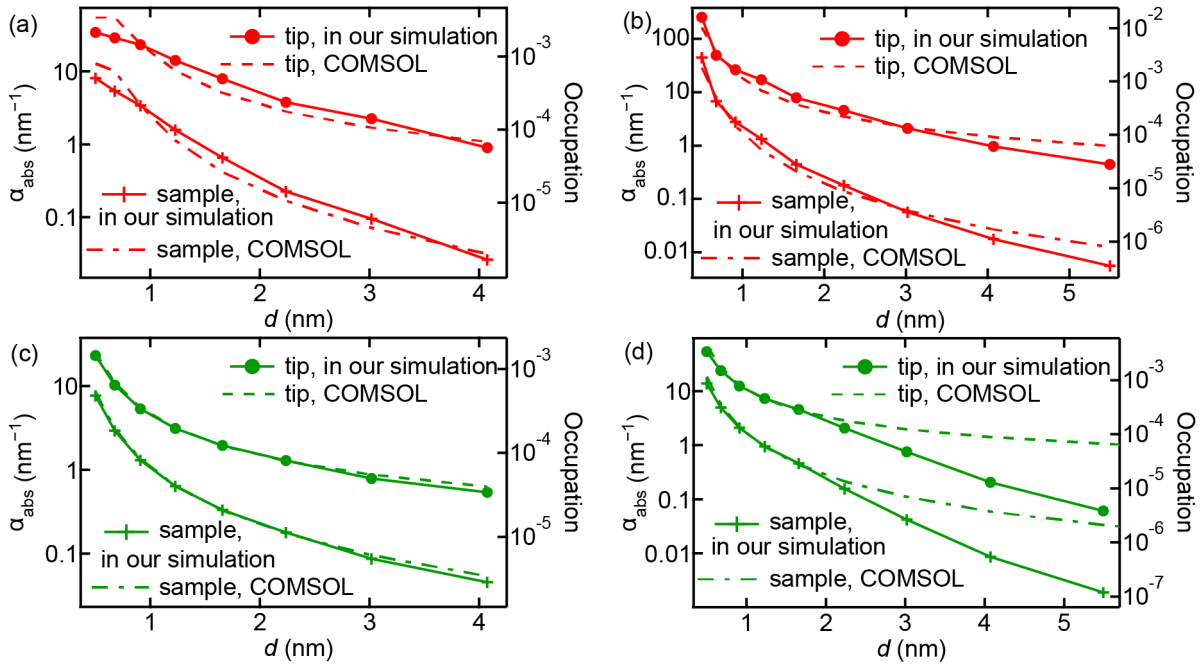

Fig. S11 coefficient α_{abs} as a function of d used in our simulations and predicted by COMSOL simulations.

Electron occupations resulting from one-photon absorption are shown in the right axes. The occupations are under the condition that the junction is excited by a laser power of 10 mW. Sources and parameters: (a) used by **Fig. 2**b, **Fig. 3**c and **Fig. 4**c; COMSOL: L_{tp}=7.5 nm and R_{tp}=3.7 nm; Excitation wavelength: 633 nm. (b) **Fig. 5** and **6**; L_{tp}=5.5 nm and R_{tp}=2.6 nm; 633 nm. (c) **Fig. 3**d; L_{tp}=4 nm and R_{tp}=4.3 nm; 532 nm. (d) **Fig. 4**d; L_{tp}=3.2 nm and R_{tp}=2.6 nm; 532 nm.

Next, we try to rationalize the α_{abs} we used via COMSOL simulations. Combining eqn S49 and S50, α_{abs} is expressed as

$$\alpha_{abs,t(s)} = \frac{1}{I_{in} V_{tp(s)}} \iiint_{V_{tp(s)}} D_{abs}(\boldsymbol{r}) dr^3 . \quad \text{(S56)}$$

The coefficients $\alpha_{abs,t}$ and $\alpha_{abs,s}$ are acquired from a three-dimensional model of STM junction depicted in the inset of Fig. 2a using COMSOL. The tip shaft has a half-opening angle of 6° and is truncated at a position 300 nm above the apex. The Ag(111) sample is modeled as a

silver layer of 100 nm thickness. The simulation is done in the electromagnetic waves, frequency domain (ewfd) interface in the wave-optic module with scattered field formulation. The background wave is a plane wave with angle and polarization indicated in **Fig. S12**a. $I_{\text{in}} = \frac{1}{2} c \varepsilon_0 F_{\text{in}}^2$, where c is speed of light, ε_0 is vacuum permittivity, F_{in} is the amplitude of the electric field of the incident light. $D_{\text{abs}}(\boldsymbol{r})$ equals to the COMSOL built-in variable ewfd.Qh. The integral volume V_{tp} and V_{s} are arbitrarily defined following the rules: the upper boundary of V_{tp} is an arc protruding upward by 0.5 nm, and the V_{s} is a hemisphere with radius equal to R_{tp} (**Fig. S12**b). Changing the rule defining the upper boundary of V_{tp} results in slight change in $\alpha_{\text{abs,t}}$, which ends up with a different L_{tp} (see next section), without changing the underlying physics. Changing the rule defining the radius of V_{s} only slightly changes the curve at V=0.5 V – 1 V, because the I^- is negligible at higher voltages. The complex refractive index of Ag is taken from the data measured by Johnson and Christy.[17]

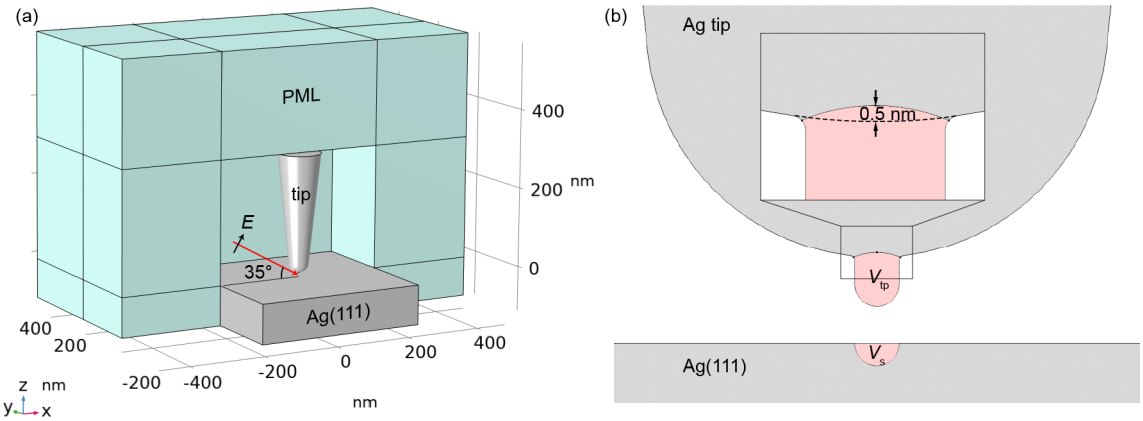

Fig. S12 COMSOL model

(a) Model used in COMSOL simulation with the perfectly matched layers (PMLs) mark by light green. (b) integration volumes V_{tp} and V_{s} (light red) for calculating $\alpha_{\text{abs,t}}$ and $\alpha_{\text{abs,s}}$.

The simulated α_{abs} from COMSOL are plotted in **Fig. S11** in comparison to the α_{abs} used in our simulations. In far-field case, the absorption coefficient for Ag is 0.085 nm^{-1} at the wavelength of 633 nm and 0.081 nm^{-1} at the wavelength of 532 nm. The 2–3 orders of magnitude enhancement in α_{abs} shown in **Fig. S11** is due to the plasmonic near-field enhancement.

In most cases, α_{abs} used in our simulation is well supported by COMSOL simulations using certain tip-protrusion length (L_{tp}), which is a free parameter. There are discrepancies at d>2 nm in **Fig. S11**d between the simulated α_{abs} from COMSOL and in our simulation. This is probably due to more complex tip shapes that our STM-junction model did not capture.

3 Analysis of shifts between FER and plasmon-assisted FER peaks

Table S2 summarizes the shift of the m-th peak between Fig. 2(a and b) in main text, defined as $\Delta V_m = V_m - V_m'$, where V_m and V_m' are the positions of the mth peak with laser off and on, respectively. For the first peak, $\Delta V_1 \approx 1.9$ V, whose value is in agreement with the value of the photon energy ($\hbar\omega = 1.96$ eV). As m increases, the shift increases substantially, reaching ~2.5 V for the fifth peak.

Table S2. peak shift (ΔV_m) in volt of the m-th peak between laser on and off. laser power: 9.5 mW, excitation wavelength: 633 nm

m	**1**	**2**	**3**	**4**	**5**
Experiment	1.9	2.3	2.4	2.5	2.5
Simulation	2.2	2.3	2.4	2.5	2.5

Table S2 also lists the simulated peak shifts. There is good agreement from the second to fifth peaks between simulation and experiment. To aid the analysis, we write the energy of the m-th FER state relative to the sample Fermi level E_m. To understand the peak shifts, we compare potential energy and the FER states at the voltage of second FER peak with and without laser excitation in Fig. 2(d and e). The second FER peak is formed when the energy of tunneling electron aligns with the second FER state, that is $eV_2=E_2$. With laser excitation in Fig. 2e, the transfer of one-photon excited hot electrons at $E_{F,t}+\hbar\omega$ dominates. Assuming E_2 is constant, there is $eV_2 = E_2 = eV_2' + \hbar\omega$, which means $\Delta V_2 = \hbar\omega/e$.

However, E_m (m≥2) exhibit significant upshift as the electrostatic field increases, similar to the energy of bound states in a triangular potential well. In a STM junction, the electrostatic field is determined by V and d. Therefore, E_2 becomes a function of V and d. With optical excitation, d is affected by P. The electrostatic field (slope of potential energy) in the condition of $V=V'_2$, P =9.5 mW in Fig. 2e is smaller than that of $V=V_2$, P=0 mW in Fig. 2d, so $E_2(V'_2$, P=9.5 mW) is lower than $E_2(V_2$, P=0), resulting in $eV_2' + \hbar\omega = E_2(V_2', P = 9.5\text{ mW}) < E_2(V_2, P = 0) = eV_2$, explaining the shift $\Delta V_2 > \hbar\omega/e$ in **Table S2**. For m>2, the difference between $E_m(V'_m$, P=9.5 mW) and $E_m(V_m$, P=0) increases because the higher m is, the more sensitive E_m is to the electrostatic field.[12]

E_1 weakly depends on the electrostatic field because it is determined largely by the image potential rather than the electrostatic field in the junction. Therefore, the shift of the first FER peak (m=1) roughly equals the value of photon energy in electron volt in experiment. However, in simulation the shift is larger than expected, likely because the model potential overestimates the change in the slope of potential energy near E_1 in response to changes in V and d.

4 Spectra curves in main figures

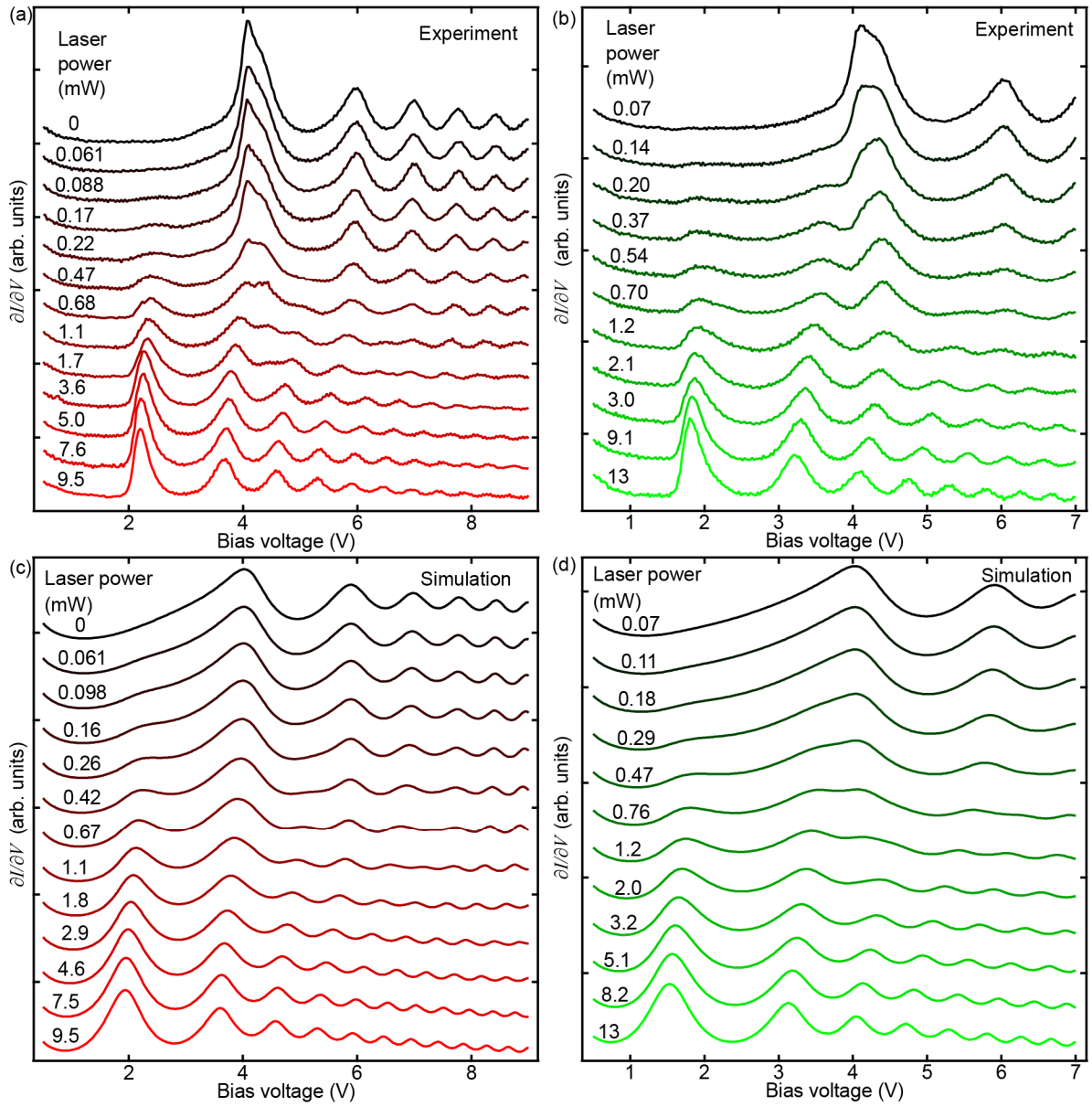

Fig. S13 Spectral curves in **Fig. 3**

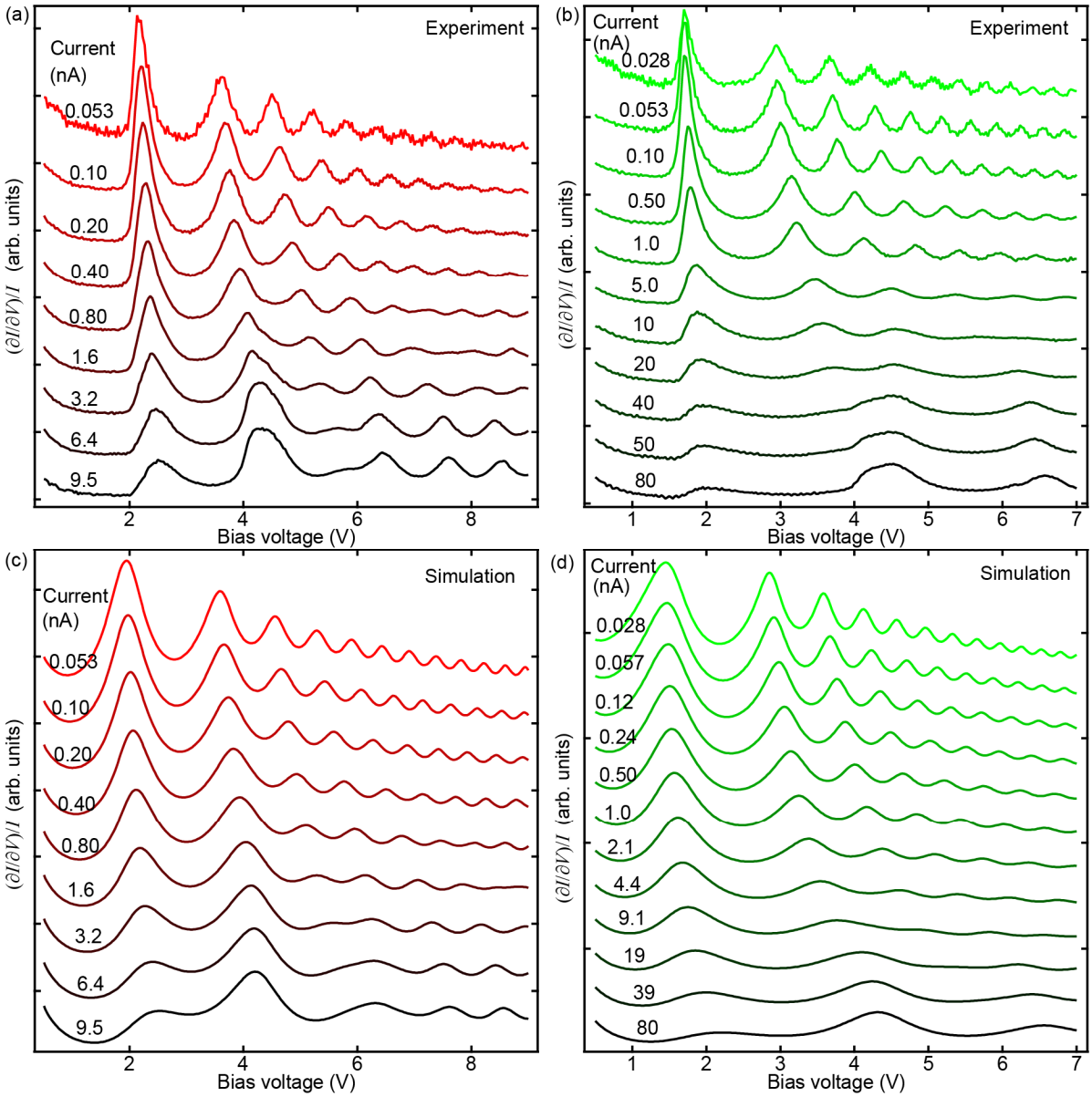

Fig. S14 Spectral curves in **Fig. 4**

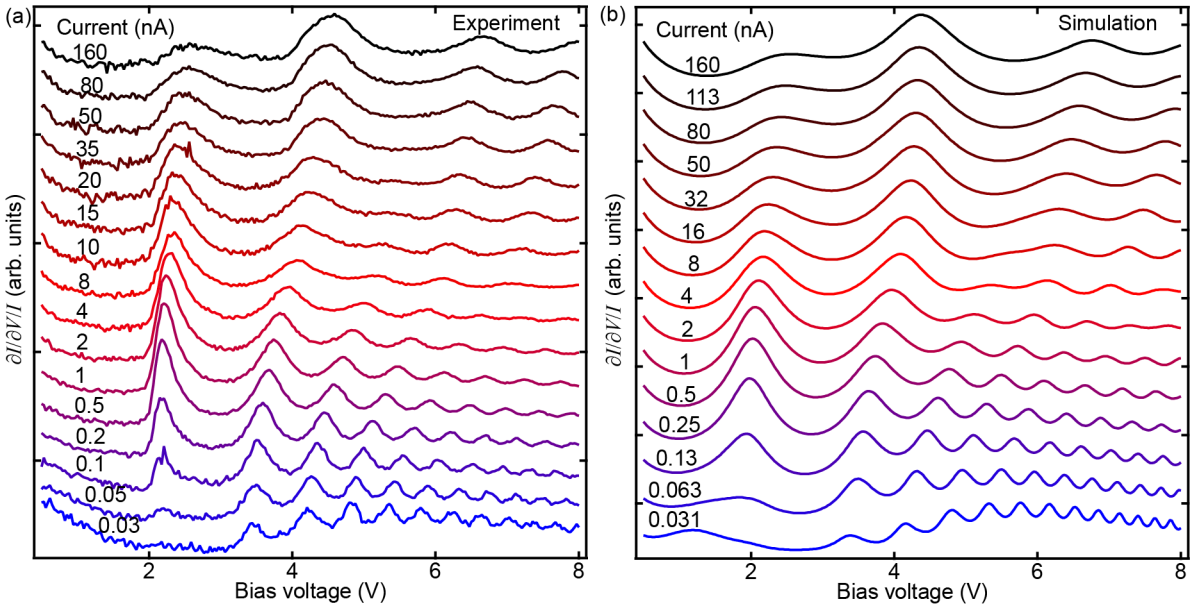

Fig. S15 Spectral curves in **Fig. 5**

5 Continuous downshift of plasmon-assisted FER peaks as laser power increases or current decreases

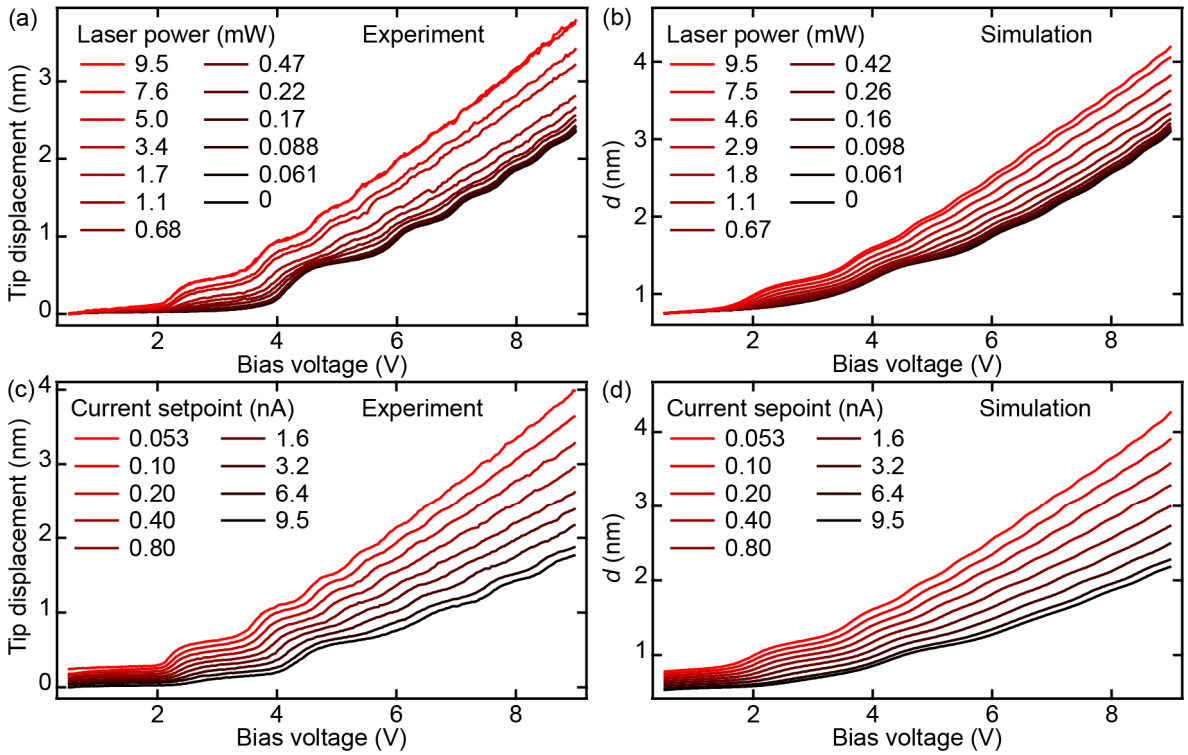

Fig. S16 Experimental tip displacements and simulated tip-sample separation as functions of bias voltage.

Each curve is acquired under a constant current condition. Positive displacement means tip retraction. Excitation wavelength: 633 nm.

In **Fig. S16**, tip–sample separation increases as laser power increases or current decreases at an arbitrary fixed voltage. This leads to decrease in electrostatic field, resulting in energy downshift of FER states (**Fig. S10**).

6 ETC transitions from n=0 to n=1 caused by laser power or current change

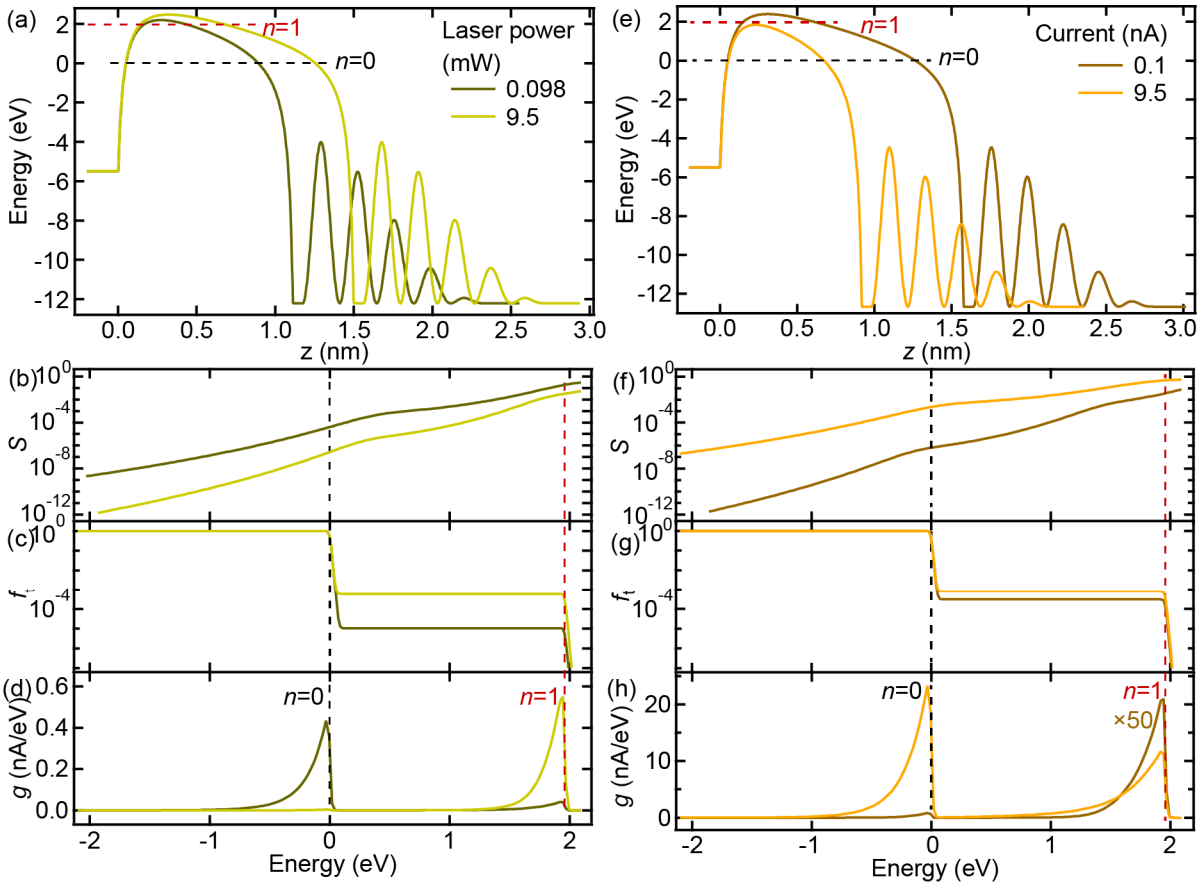

Fig. S17 Evolution of potential energy curves, transmission coefficients (S), tip electron distribution functions (f_t), and energy distribution of current (g) as laser power or current changes.

All energies are relative to tip Fermi level. The black dashed lines indicate the n=0 ETC near tip Fermi level ($E_{F,t}$), and red dashed lines indicate the n=1 ETC near the energy level of $E_F+\hbar\omega$, respectively. Excitation wavelength: 633 nm; (a–d) V=3.75 V, I=100 pA; (e–h) V=4.2 V, laser power: P=5.5 mW.

As laser power increases, tip–sample separation increases, and potential barrier width increases (**Fig. S17**a). This causes ratio of transmission coefficients $S(E_F+\hbar\omega)/S(E_{F,t})$ increase (**Fig. S17**b). On the other hand, $f_t(E_F+\hbar\omega)$ also increases (**Fig. S17**c). As a result, at low laser power, current is distributed mainly in n=0 ETC, while at high laser power, current is distributed mainly in n=1 ETC (**Fig. S17**d).

As current increases, tip–sample separation decreases, and potential barrier width decreases (**Fig. S17**e). This causes ratio of transmission coefficients $S(E_F+\hbar\omega)/S(E_{F,t})$ decrease (**Fig. S17**f). On the other hand, $f_t(E_F+\hbar\omega)$ increases (**Fig. S17**g). At low current, current is

distributed mainly in n=1 ETC (**Fig. S17**h). The simulations show that the effect of S-ratio change is stronger than the effect of f_t change, so at high current, the current fraction in n=0 ETC surpasses that in n=1 ETC.

7 Confirming the assignment of peaks labeled 1–4 in Fig. 4a to n=0 ETC

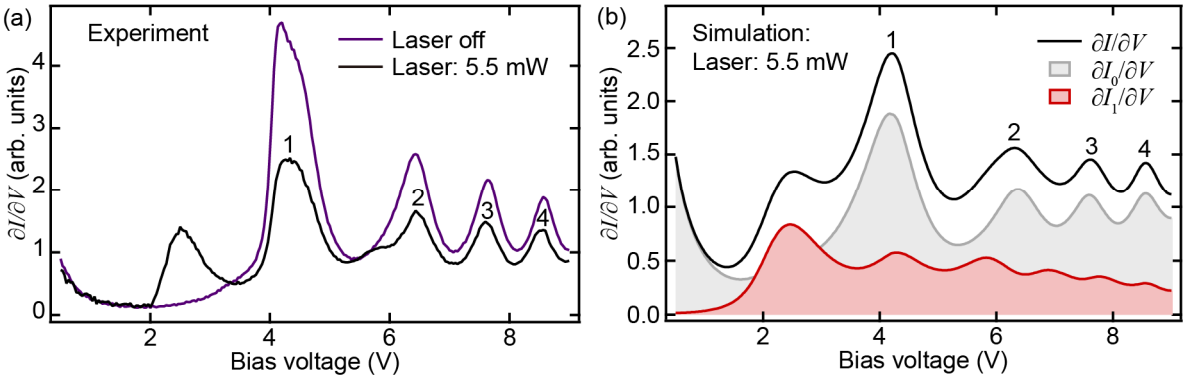

Fig. S18 Confirming the assignment of peaks labeled 1–4 in **Fig. 4**a to n=0 ETC.
(a) Comparison of the DCS at I=9.5 nA in **Fig. 4**a with a DCS acquired in dark condition (I=8 nA). (b) Simulated DCS at I=9.5 nA and differential conductance originating from n=0 and n=1 ETC. Excitation wavelength: 633 nm.

The experimental results in **Fig. S18**a show that the positions of peaks 1–4 coincide with the first to fourth FER peaks in the dark condition at I=8 nA, so they are assigned as FER peaks. The simulated results in **Fig. S18**b show that peaks 1–4 originate from n=0 ETC, confirming the assignment.

8 Understanding sloped background in DCS arising from n=2 photoemission

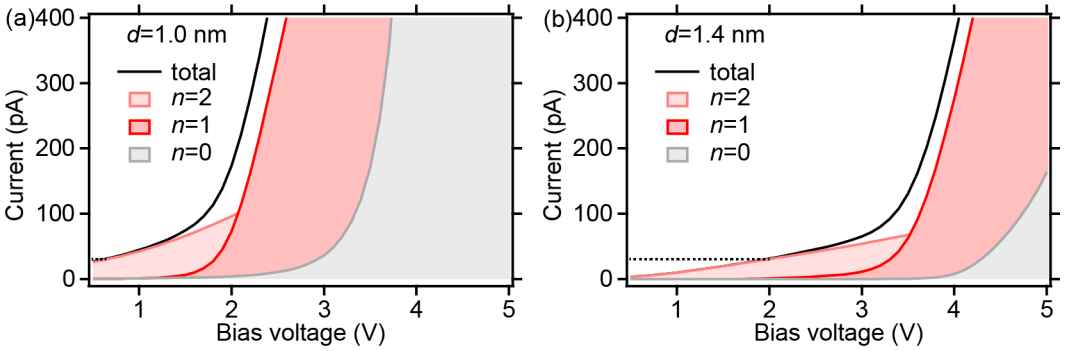

Fig. S19 Current–bias voltage curves at d=1.0 nm and 1.4 nm for the simulations in Fig. 5c. The dotted line mark I=30 pA.

In simulations, the $\partial I/\partial V$ is evaluated under fixed d, because under fixed I, $\partial I/\partial V \equiv 0$. In experiment, the situation is in between those two extremes, because the feedback cannot fully suppress current fluctuations caused by modulating bias voltage. Therefore, one should examine I–V curves under constant d to understand the sloped background in DCS arising from n=2 photoemission.

In **Fig. S19**, I_2 increases more rapidly as bias voltage increases at smaller d. As a result, the slope ($\partial I/\partial V$) at I=30 pA is larger at smaller d, explaining the sloped background in Fig. 5c.

9 Comparison between experimental and simulated current–distance curves

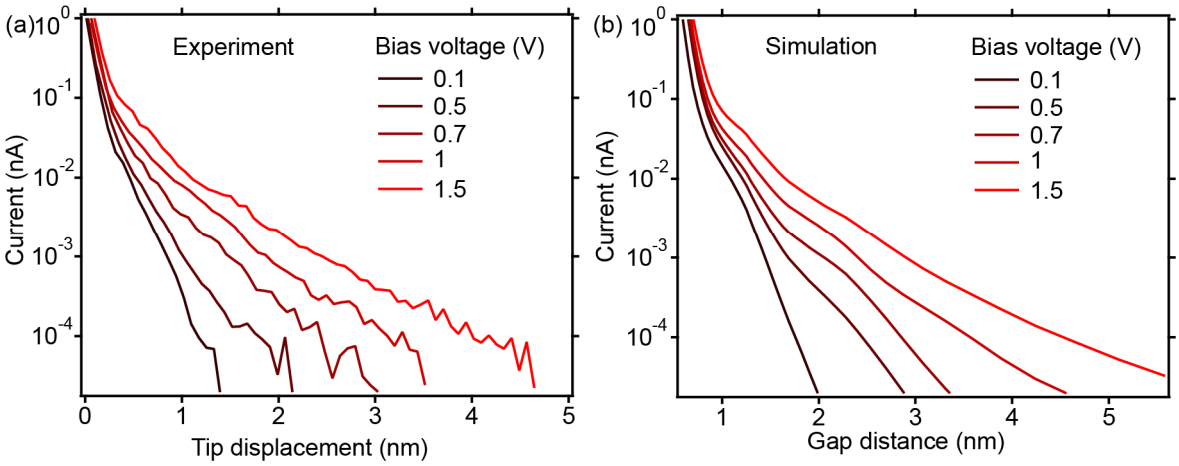

Fig. S20 Comparing experimental and simulated current–distance curves from **Fig. 6** (633 nm).

Fig. S20 shows that the simulated current–distance curves at V=0.1–1.5 V from Fig. 6 agree with the experimental curves.

In **Fig. S21**(a and b), we show experimental and simulated current–distance curves at an excitation wavelength of 532 nm. The simulated curves generally agree with the experimental ones. Both experimental and simulated curves show distinct decay constant β in different sections. **Fig. S21**(c–e) show the origin of the decay constant changes. At V=0.5 V, the dominant electron transfer transit from n=0 to n=2 process without being through the n=1 process as gap distance increases. At V=1.8 V where the first plasmon-assisted FER peak is located, n=1 process becomes dominant in between the regions where n=0 and n=2 processes dominate. The region where n=1 process dominates is enlarged at V=4 V.

In the insets of **Fig. S21**(a and b), we find that the decay constant β at 100 pA decreases step-by-step as bias voltage increases, and that the arrival of new steps coincides with the plasmon-assisted FER peaks. The first drop of β at around V=1.5 V is due to transition of

electron tunneling from n=0 to 1 process. The second and third drops at around V=2.8 V and around 3.8 V is associated with the second and the third FER states, respectively. This phenomenon relates to the findings that the decay constant, or apparent barrier height, is affected by the features in the local density of states versus energy.[7] The simulations in the inset of **Fig. S21**b successfully reproduce this phenomenon, warranting simulation results.

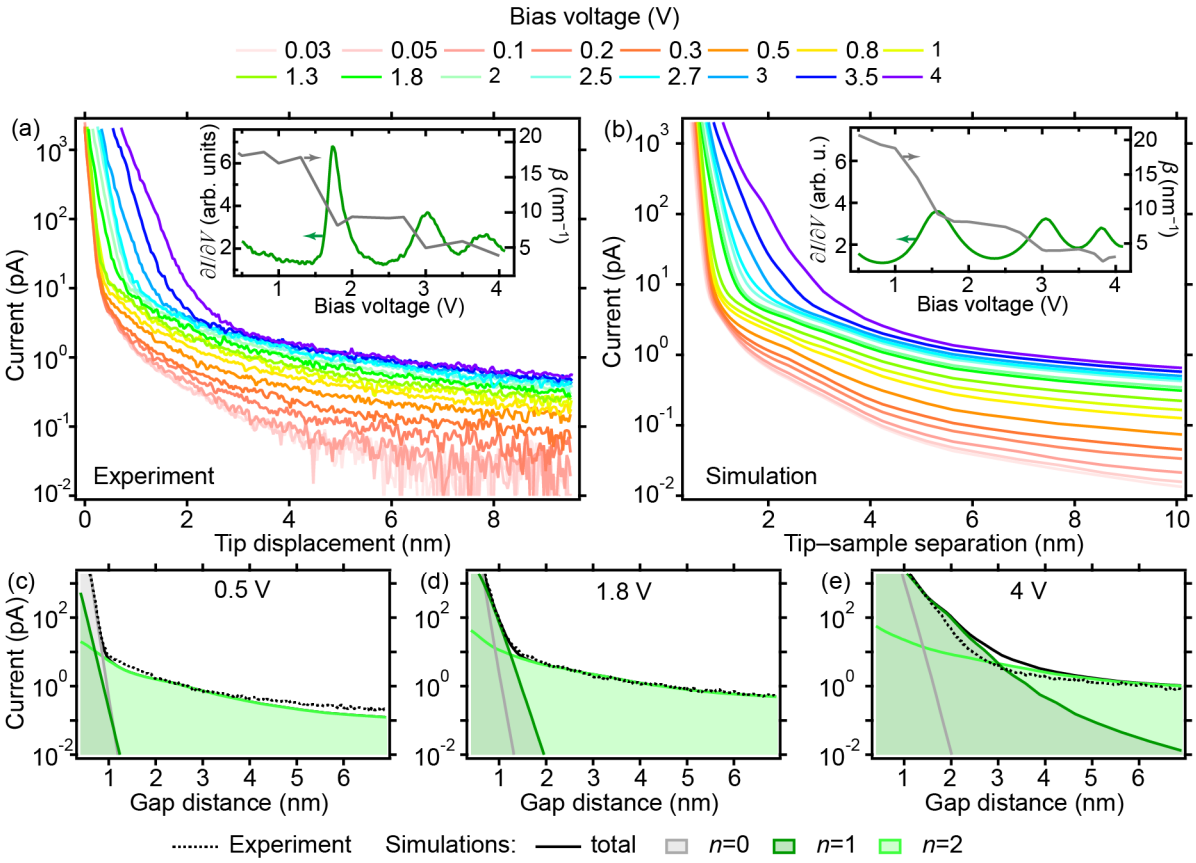

Fig. S21 Experimental and simulated current–distance curves at an excitation wavelength of 532 nm.

Insets: left axis: DCS acquired together with the current–distance curves at I=100 pA, right axis: decay constant β at I=100 pA versus bias voltage. Laser power: 15 mW, Simulation parameters: R_{tp}=2.1 nm and α_{abs} used in the simulations is provided in **Fig. S22**. (c–e) Experimental and simulated current–distance curves and simulated current curves from n=0, 1, and 2 electron transfer processes at three selected voltages.

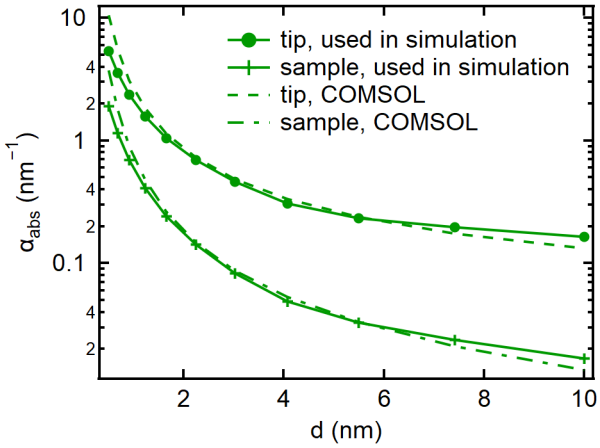

Fig. S22 α_{abs} used in the simulations in **Fig. S21** and predicted by COMSOL with L_{tp}=1 nm, R_{tp}=2.1 nm and λ=532 nm.

10 Simulated laser-power dependence of DCS with *n*=2 ETC

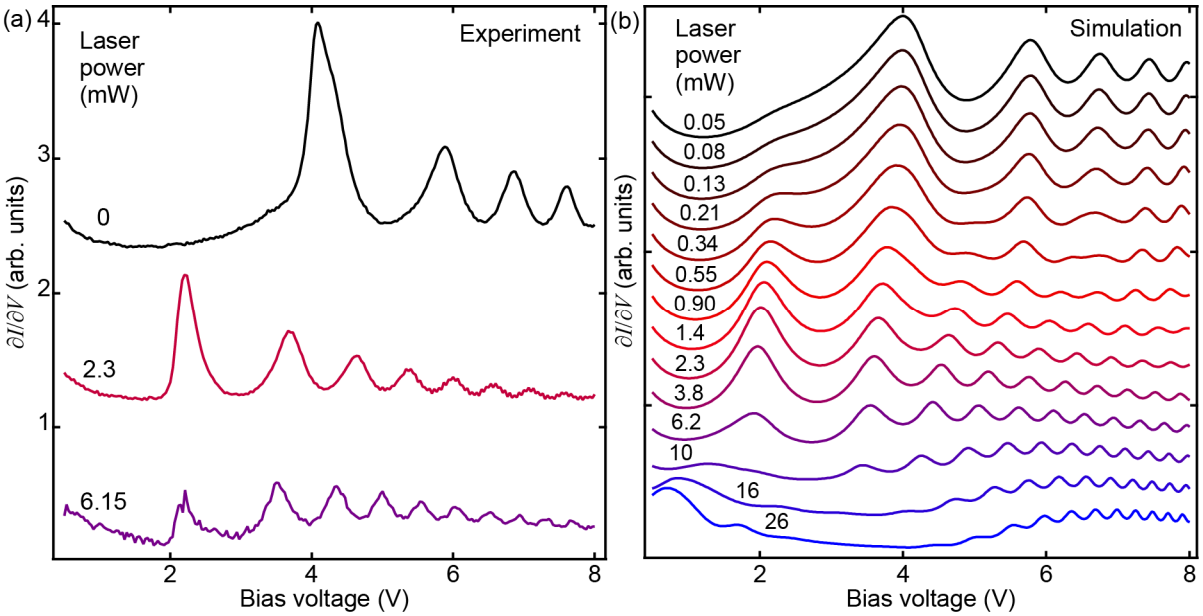

Fig. S23 Simulated differential conductance spectra (DCS) and transition of electron transfer processes from *n*=0, 1, to *n*=2 as laser power increases corresponding to the simulations in **Fig. 5**.

(a, b) DCS at *I*=100 pA (c) DCS at *P*=16 mW and differential conductance originating from *n*=0, 1, and 2 electron transfer processes. (d) current fraction from *n*=0, 1 and 2 electron transfer processes presented by the intensity of red, green, and blue channels in a RGB color, respectively. Excitation wavelength: 633 nm.

References

1. G. N. Derry, M. E. Kern and E. H. Worth, Recommended values of clean metal surface work functions, *Journal of Vacuum Science & Technology A: Vacuum, Surfaces, and Films*, 2015, **33**, 060801 DOI: 10.1116/1.4934685.
2. W. R. Smythe, *Static and Dynamic Electricity*, Taylor & Francis, Third Edition edn., 1989.
3. T. Laloyaux, I. I. Derycke, J. Vigneron, P. Lambin and A. A. Lucas, Simulation of current in the scanning tunneling microscope, *Phys Rev B Condens Matter*, 1993, **47**, 7508-7518 DOI: 10.1103/physrevb.47.7508.
4. J. G. Simmons, Potential Barriers and Emission‐Limited Current Flow Between Closely Spaced Parallel Metal Electrodes, *J. Appl. Phys.*, 1964, **35**, 2472-2481 DOI: 10.1063/1.1702884.
5. H.-C. Ploigt, C. Brun, M. Pivetta, F. Patthey and W.-D. Schneider, Local work function changes determined by field emission resonances:NaCl / Ag(100), *Phys. Rev. B*, 2007, **76**, 195404 DOI: 10.1103/PhysRevB.76.195404.
6. H. Wern, R. Courths, G. Leschik and S. Hüfner, On the band structure of silver and platinum from angle-resolved photoelectron spectroscopy (ARUPS) measurements, *Zeitschrift für Physik B Condensed Matter*, 1985, **60**, 293-310 DOI: 10.1007/BF01304449.
7. M. Becker and R. Berndt, Influence of band structure on the apparent barrier height in scanning tunneling microscopy, *Phys. Rev. B*, 2010, **81**, 035426 DOI: 10.1103/PhysRevB.81.035426.
8. C. Lin, F. Krecinic, H. Yoshino, A. Hammud, A. Pan, M. Wolf, M. Müller and T. Kumagai, Continuous-Wave Multiphoton-Induced Electron Transfer in Tunnel Junctions Driven by Intense Plasmonic Fields, *ACS Photonics*, 2023, **10**, 3637-3646 DOI: 10.1021/acsphotonics.3c00714.
9. V. T. Binh, N. Garcia and S. T. Purcell, in *Advances in Imaging and Electron Physics*, ed. P. W. Hawkes, Elsevier, 1996, vol. 95, pp. 63-153.
10. J. G. Simmons, Generalized Formula for the Electric Tunnel Effect between Similar Electrodes Separated by a Thin Insulating Film, *J. Appl. Phys.*, 1963, **34**, 1793-1803 DOI: 10.1063/1.1702682.
11. N. V. Smith, C. T. Chen and M. Weinert, Distance of the image plane from metal surfaces, *Phys Rev B Condens Matter*, 1989, **40**, 7565-7573 DOI:

10.1103/physrevb.40.7565.

12. T. Kumagai, S. Liu, A. Shiotari, D. Baugh, S. Shaikhutdinov and M. Wolf, Local electronic structure, work function, and line defect dynamics of ultrathin epitaxial ZnO layers on a Ag(1 1 1) surface, *J Phys Condens Matter*, 2016, **28**, 494003 DOI: 10.1088/0953-8984/28/49/494003.
13. Y. Dubi, I. W. Un and Y. Sivan, Distinguishing Thermal from Nonthermal ("Hot") Carriers in Illuminated Molecular Junctions, *Nano Lett.*, 2022, **22**, 2127-2133 DOI: 10.1021/acs.nanolett.1c04291.
14. N. Del Fatti, C. Voisin, M. Achermann, S. Tzortzakis, D. Christofilos and F. Vallée, Nonequilibrium electron dynamics in noble metals, *Phys. Rev. B*, 2000, **61**, 16956-16966 DOI: 10.1103/PhysRevB.61.16956.
15. Y. Sivan and Y. Dubi, Theory of "Hot" Photoluminescence from Drude Metals, *ACS Nano*, 2021, **15**, 8724-8732 DOI: 10.1021/acsnano.1c00835.
16. E. D. Fung, O. Adak, G. Lovat, D. Scarabelli and L. Venkataraman, Too Hot for Photon-Assisted Transport: Hot-Electrons Dominate Conductance Enhancement in Illuminated Single-Molecule Junctions, *Nano Lett.*, 2017, **17**, 1255-1261 DOI: 10.1021/acs.nanolett.6b05091.
17. P. B. Johnson and R. W. Christy, Optical Constants of the Noble Metals, *Phys. Rev. B*, 1972, **6**, 4370-4379 DOI: 10.1103/PhysRevB.6.4370.